REPORT DOCUMENTATION PAGE	Form Approved OMB NO. 0704-0188

1. REPORT DATE (DD-MM-YYYY) 20-11-2019	2. REPORT TYPE Final Report	3. DATES COVERED (From - To) 1-Sep-2016 - 31-Aug-2019

4. TITLE AND SUBTITLE Final Report: Mathematical and Multi-Scale Foundations of Nonlocal Modeling: Research Topic 1.2 Solid Mechanics W911NF-12-R-0012-03	5a. CONTRACT NUMBER W911NF-16-1-0456
	5b. GRANT NUMBER
	5c. PROGRAM ELEMENT NUMBER 611102
6. AUTHORS	5d. PROJECT NUMBER
	5e. TASK NUMBER
	5f. WORK UNIT NUMBER

7. PERFORMING ORGANIZATION NAMES AND ADDRESSES

Louisiana State University and A&M Colle
Office of Sponsored Programs
202 Himes Hall
Baton Rouge, LA 70803 -0001

8. PERFORMING ORGANIZATION REPORT NUMBER

9. SPONSORING/MONITORING AGENCY NAME(S) AND ADDRESS (ES)

U.S. Army Research Office
P.O. Box 12211
Research Triangle Park, NC 27709-2211

10. SPONSOR/MONITOR'S ACRONYM(S)
ARO

11. SPONSOR/MONITOR'S REPORT NUMBER(S)
68760-EG.32

12. DISTRIBUTION AVAILIBILITY STATEMENT
Approved for public release; distribution is unlimited.

13. SUPPLEMENTARY NOTES
The views, opinions and/or findings contained in this report are those of the author(s) and should not contrued as an official Department of the Army position, policy or decision, unless so designated by other documentation.

14. ABSTRACT

15. SUBJECT TERMS

16. SECURITY CLASSIFICATION OF:			17. LIMITATION OF ABSTRACT	15. NUMBER OF PAGES	19a. NAME OF RESPONSIBLE PERSON Robert Lipton
a. REPORT UU	b. ABSTRACT UU	c. THIS PAGE UU	UU		19b. TELEPHONE NUMBER 225-578-1569

RPPR Final Report
as of 06-Jan-2020

Agency Code:

Proposal Number: 68760EG **Agreement Number: W911NF-16-1-0456**

INVESTIGATOR(S):

Name: Robert Lipton
Email: lipton@lsu.edu
Phone Number: 2255781569
Principal: Y

Organization: **Louisiana State University and A&M College**
Address: Office of Sponsored Programs, Baton Rouge, LA 708030001
Country: USA

DUNS Number: 075050765 EIN: 726000848
Report Date: 30-Nov-2019 Date Received: 20-Nov-2019
Final Report for Period Beginning 01-Sep-2016 and Ending 31-Aug-2019
Title: Mathematical and Multi-Scale Foundations of Nonlocal Modeling: Research Topic 1.2 Solid Mechanics W911NF-12-R-0012-03
Begin Performance Period: 01-Sep-2016 **End Performance Period:** 31-Aug-2019
Report Term: 0-Other
Submitted By: Robert Lipton Email: lipton@lsu.edu
Phone: (225) 578-1569
Distribution Statement: 1-Approved for public release; distribution is unlimited.

STEM Degrees: 2 **STEM Participants:** 3

Major Goals: The proposed research embarks on a systematic and coordinated analysis of nonlocal constitutive laws for fracture modeling. The proposed work will develop the mathematical foundations that will further the use of nonlocal continuum models as reliable computational tools for fracture modeling. The approach taken here is new and is based on a mathematically rigorous development of peridynamic models with convex-concave energies. These energies are well suited to nonlocal formulations of peridynamic type in both state based and bond based models. The thrust of the proposed research is to develop theoretical and mathematically rigorous connections between the new nonlocal models with convex-concave energies and classic brittle fracture models. The first goal will seek to show that smooth solutions of the nonlocal model converge to the solution of the linear elastic wave equation as the length scale of nonlocal interaction goes to zero. Here we will provide convergence rates given in terms of the length of nonlocal interaction. A second goal is to provide a stable and consistent numerical scheme for the nonlocal evolution of smooth solutions. A third goal will develop convergence rates for nonlocal evolutions to known fracture solutions. The fourth goal is to develop a stable and consistent numerical scheme for nonlocal fracture modeling. The final objective is to develop a fundamentally sound quasi-static limit of nonlocal dynamics for reliable modeling of quasi-static crack growth. In all cases the primary interest is to explore and rigorously determine the range of validity for nonlocal models contingent on the physical dimensions of the sample, length scale of nonlocal interaction, material properties and characteristics of the loading. The overall goal of this effort is to establish the theoretical foundations necessary for nonlocal models to provide reliable and predictive numerical fracture simulations for problems of brittle fracture.

Accomplishments: We have accomplished the first goal of the proposed research and have theoretically demonstrated the convergence of smooth solutions of the nonlocal model to solutions of the linear balance of momentum equation for elasticity. We establish that the rate of convergence is proportional to the length scale of nonlocal interaction as it tends to zero. We go on to accomplish the second goal and develop a stable finite difference numerical method for this case. We show that if the length scale of the finite difference scheme tends to zero faster than the nonlocal interaction length scale we numerically recover the classic evolution given by the linear balance of momentum equation. This is reported in the publication written together by myself and the grant supported postdoc Prashant Jha, titled "Numerical convergence of nonlinear nonlocal continuum models to local elastodynamics" published in the International Journal of Numerical Methods in Engineering, 114, (2018), pp. 1389–1410.

To accomplish the third goal we have established the explicit relationship between solutions of the nonlocal models introduced in this proposal and the classic fracture solutions articulated in Freund (Dynamic Fracture Mechanics, Cambridge Univ. Press, 1990). To understand what is going on the PI uses the nonlocal models obtained from double well potentials developed under this grant support. In this framework the nonlocal balance of momentum equation is viewed as a mesoscale model that includes details of both elastic interaction and process zone encoded into the force potential. It is shown mathematically by the PI that fracture appears as an emergent phenomena at the macroscale generated by an underlying peridynamic field theory at the mesoscale eliminating the need for supplemental kinetic relations describing crack growth. Methods of applied mathematics are used to show that the time evolution of the deformation for these models converge with vanishing non-locality to an evolving deformation u(x,t) crack set J(x,t) pair. The deformation u(x,t) suffers jumps across the crack set J(x,t) and the linear balance of momentum holds away from the crack set. Here the linear elastic tensor, energy release rate and strength of the material is contained inside the force potential. Under this grant support it is shown that the interaction between a sharp crack and intact material can be deduced in the limit of vanishing non-locality directly from the nonlocal dynamics. This interaction agrees with the modern theory of fracture mechanics for running cracks. This is established mathematically using well posed variational methods together with the notion of weak convergence. In addition it is shown that the time rate of change of internal energy of any subdomain surrounding the crack tip can be written as an expansion in the diameter of the domain. To leading order it is the difference between the power consumed by the growing crack in terms of the material's critical energy release rate and the power being supplied to the domain by the motion of the elastic media surrounding the crack tip. We recover the generalization of Griffith's criterion to dynamic fracture mechanics and the associated kinetics governing the crack tip velocity. The modern theory of dynamic fracture mechanics articulated in Freund uses Mott's hypotheses on the power balance around the crack tip to facilitate recovery of the crack tip kinetic relation; however using the nonlocal model the same kinetic relation is recovered directly in the limit of vanishing non-locality and Mott's hypothesis is no longer a hypothesis but is instead a consequence the nonlocal modeling. This paper is currently in preprint from on arXiv.org at https://arxiv.org/abs/1908.07589 and will be submitted for publication as two articles.

We have attained the fourth goal and have developed stable and consistent numerical schemes for nonlocal fracture modeling for nonlocal models associated with two and three dimensional fracture problems. The first accomplishment in this direction are the first upper bounds on the convergence rate of finite difference approximations for nonlocal fracture given by bond based peridynamic models. Finite difference methods have been used as simulation tools for peridynamic models since 2000, see (Silling JMPS 48 (2000), pp. 175-209). We consider two point force interactions characterized by a double well potential. This type of interaction is known popularly as bond based peridynamics. We show the existence of an evolving Holder continuous displacement field. A special case are Lipschitz continuous solutions with, |u(x)-u(y)|<C|x-y|, where u is the displacement, x and y are points, and C is a constant independent of u, x, and y. For Lipschitz continuous solutions the rate of convergence is on the order (d+ h/epsilon^2) where epsilon gives the length scale of nonlocal interaction, h is the discretization length and d is the time step. This rate is uniform in time for bounded time intervals. It is shown that the rate of convergence holds for both the forward Euler scheme as well as general single step implicit schemes. The Holder continuous evolution converges to a brittle fracture evolution in the limit of epsilon going to zero. These are the first (and still only) error estimates for finite difference approximations to nonlinear and nonlocal fracture models of peridynamic type. This research work has appeared in ``Numerical Analysis of Nonlocal Fracture Models in Holder Space,'' by Prashant Jah and Robert Lipton, SIAM Journal on Numerical Analysis, 56 (2018), pp. 906--941.

The second accomplishment along these lines are the first upper bounds on the convergence rate of finite difference approximations for nonlocal fracture given by state based peridynamic models. These results extend earlier supported work to materials that can fail due to cavitation and subsequent fracture. Here the nonlocal model is initially elastic but beyond a critical strain the material softens with increasing strain. This model is formulated as a state-based peridynamic model using two potentials: one associated with hydrostatic strain and the other associated with tensile strain. We show the existence of an evolving Lipshitz continuous displacement field. For Lipschitz continuous solutions the rate of convergence is order (d+ h/epsilon^2) where epsilon gives the length scale of nonlocal interaction, h is the discretization length and d is the time step. It is shown that this rate of convergence holds for both the forward Euler scheme as well as general single step implicit schemes. The Lipchitz continuous evolutions converge to a brittle fracture evolution in the limit of vanishing non-locality. These are the first error estimates for finite difference approximations to state based fracture models of peridynamic type. Numerical experiments demonstrate that the rate of increase in peridynamic energy of the evolving fracture region is the same as the classical Griffith energy release rate. This work is published with Prashant Jha in Computer Methods in Applied Mechanics and Engineering 351 (2019), pp. 184–225.

Last we establish a better convergence rate for the finite element scheme for the state based nonlocal model with regularized solutions. The convergence rate is of the order (d+ h^2/epsilon^2) where epsilon gives the length scale of nonlocal interaction, h is the discretization length and d is the time step. Numerical experiments show that the rate of increase in peridynamic energy of the evolving fracture region is the same as the Griffith energy release rate. We show that regularized solutions converge to brittle fracture evolution in the limit of vanishing non-locality. Here the slopes of these regularized solutions steepen and become jumps in the limit of vanishing non-locality. This work is published with Prashant Jha in Communications on Applied Mathematics and Computation (2019). https: //doi.org/10.1007/s42967.

Training Opportunities: This grant supported the postdoctoral research of Dr. Prashant Jha. While on this grant Dr. Jha was an active participant in the research work that lead to 6 scientific publications 4 book chapters, 2 preprints submitted for publication and one scientific paper now in preparation. I met with Dr. Jha twice per week for the past 3 years. During our meetings we reviewed mechanics literature and I taught him the mathematics of the finite difference and finite element approximations, methods of variational convergence, and general functional and numerical analysis. Since finishing the grant in August 2019, Dr. Jha is now a Postdoctoral Fellow at the Oden Institute at the University of Texas. This grant also supported Dr. Patrick Deihl who is is a postdoc working on the parallel numerical implementation of the nonlocal model developed here. His participation is central to the parallelization of this numerical method and has participated on one preprint submitted for publication.

RPPR Final Report
as of 06-Jan-2020

Results Dissemination: Research results and products have been disseminated through lectures at scientific conferences, academic institutions and DoD labs. Results have also been disseminated through scientific articles appearing in top Numerical Analysis and computational Mechanics Journals a listing of all publications as of this date are given below the lecture section as well as in the products pod.

Outreach has been accomplished through the invited lectures listed below.

Invited talk: Double Well Potentials and Brittle Fracture Modeling. Given at Wright Patterson Air Force Base, Wright Patterson Labs, Materials and Manufacturing Directorate, August 14-18, 2017.

``Double Well Potentials and Nonlocal Brittle Fracture Modeling." Aerospace Engineering Seminar, University of Texas, September 28, 2017.

``Nonlocal Models for Complex Fracture Simulations." Babuska Seminar, ICES, University of Texas, October 20, 2017.

``Damage with memory: a non-local state based model," Nonlocal Methods for Fracture, ICES, University of Texas, January 15-16, 2018.

``Damage with Memory: A Non-Local State Based Model.'' Engineering Mechanics Institute Conference Massachusetts Institute of Technology, May 27-31, 2018.

``Double Well Potentials and Nonlocal Brittle Fracture Modeling." Fields Institute, Toronto Canada, Conference in Multiscale Problems in Materials and Biology, June 4-7, 2018.

``Free Damage Propagation with Memory,” 13th World Congress on Computational Mechanics (WCCM XIII), July 22-27, 2018 New York, New York.

``Predicting Complex Fracture Evolution using Nonlocal Dynamics," Department of Mathematics, Colloquium, University of Nebraska, Lincoln Nebraska, September 14, 2018.

``Complex Fracture Evolution using Nonlocal Dynamics," Department of Mechanical Engineering, Graduate Student Seminar, University of Nebraska, Lincoln Nebraska, September 13, 2018.

``Nonlocal Brittle Fracture Modeling," Mathematical Aspects of Materials Science Mini-symposium at the MRS Spring Meeting, April 22--26, 2019, Phoenix, AZ.

``Nonlocal Models for Computing Dynamic Fracture," CFRAC 2019 - VI International Conference on Computational Modeling of Fracture and Failure of Materials and Structures, June 12-14, 2019, Braunschweig, Germany.

``Nonlocal Models for Computing Dynamic Fracture," Engineering Mechanics Institute Conference, June 18-21, 2019, Caltech, Pasadena, CA

``Convergence Results for Finite Element and Finite Difference Approximation of Nonlocal Fracture Models,"ICIAM 2019 - International Congress on Industrial and Applied Mathematics, July 15-19, 2019, Valencia Spain.

``Nonlocal Brittle Fracture Modeling," ICIAM 2019 - International Congress on Industrial and Applied Mathematics, July 15-19, 2019, Valencia Spain.

``Numerical Fracture Experiments using Nonlocal Fracture Models," USNCCM 2019 - U.S. National Congress on Computational Mechanics, July 28-30, 2019, Austin, TX.

``Nonlocal Models for Computing Dynamic Fracture," USNCCM 2019 - U.S. National Congress on Computational Mechanics, July 28-30, 2019, Austin, TX.

Journal Publications of ARO supported research (to date):

Jha, P. and Lipton, R.,``Numerical convergence of nonlinear continuum models to local elastodynamics.''

International Journal of Numerical Methods in Engineering. Published March 12, 2018, https://doi.org/10.1002/nme.5791.

Lipton, R., Said, E., and Jha, K. ``Free damage propagation with memory.'' Journal of Elasticity. Published March 14, 2018, https://doi.org/10.1007/s10659-018-9672-7.

Jha, P. and Lipton, R., ``Numerical analysis of nonlocal fracture models in Holder space.'' SIAM Journal on Numerical Analysis 56 (2018), pp. 906-941.

P. K. Jha and R. P. Lipton, Numerical convergence of finite difference approximations for state based peridynamoc fracture
models. Computer Methods in Applied Mechanics and Engineering, 351 (2019) 184-225.

P.K. Jha and R. P. Lipton, Finite element convergence for state based peridynamic fracture models. Communications on Applied Mathematics and Computation, 31, May 2019 doi/10.1007/s42967-019-00039-4.

R. P. Lipton, R. B. Lehoucq and P.K. Jha, Complex fracture nucleation and evolution with nonlocal elastodynamics, Journal of Peridynamics and Nonlocal Modeling, 5 April 2019, doi/10.1007/s42102-019-00010-0.

Preprints submitted for publication in peer reviewed journals:

R.P. Lipton and P.K. Jha, Classic dynamic fracture recovered as the limit of a nonlocal peridynamic model: The single edge notch in tension. ArXiv.org; arXiv:1908.07589v1 [math.AP] 20 Aug. 2019.

P. Diehl, P.K. Jha, H. Kaiser, R. Lipton, and M. Levesque, Implementation of peridynamics utilizing HPX – the C++ standard library for parallelism and concurrency. ArXiv.org; arXiv:1806.06917v2 [cs.DC] 27 Aug. 2019.

Honors and Awards: Robert Lipton has been named Fellow of the American Mathematical Society, member of the 2020 class of AMS Fellows.

Protocol Activity Status:

Technology Transfer: Visited Wright Patterson Air Force Base, Wright Patterson Labs, Materials and Manufacturing Directorate, August 14-18, 2017. Invited talk: Double Well Potentials and Brittle Fracture Modeling. Spoke with Dr. Craig Przybyla Composite Performance Team Leader. Discussed numerical convergence of nonlocal schemes and application to coated fiber composites.

PARTICIPANTS:

Participant Type: Postdoctoral (scholar, fellow or other postdoctoral position)
Participant: Prashant Kumar Jha
Person Months Worked: 12.00 **Funding Support:**
Project Contribution:
International Collaboration:
International Travel:
National Academy Member: N
Other Collaborators:

Participant Type: Postdoctoral (scholar, fellow or other postdoctoral position)
Participant: Patrick Diehl
Person Months Worked: 1.00 **Funding Support:**
Project Contribution:
International Collaboration:
International Travel:
National Academy Member: N
Other Collaborators:

RPPR Final Report

as of 06-Jan-2020

Final Report:

Mathematical and Multiscale Foundations of Nonlocal Modeling

Army Research Office Grant
W911NF-16-0456

Robert Lipton
Department of Mathematics
Louisiana State University
Baton Rouge, LA 70803, USA
`lipton@math.lsu.edu`

Contents

Chapter 1

Introduction

1.1 Overview

The goals of the grant supported project have been achieved for a significant class of nonlocal fracture models. The advantage of nonlocal modeling is that fracture becomes an emergent phenomena in an another wise elastic material and the dynamics is mediated only by the balance of linear momentum. This obviates any need for supplementary kinetic relations describing the crack motion. In the project we have developed the theory of numerical analysis for a nonlocal theory of fracture mechanics that can be categorized as a generic state-based peridynamic theory [Silling, 2000, Silling et al., 2007]. The strain inside the medium is expressed in terms of displacement differences as opposed to the displacement gradients. Acceleration of a point is due to the sum of the forces acting on the point from near by points. Here fracture emerges from the nonlocal dynamics. The nonlocal model has been applied numerically to model fracture phenomenon in materials, see for example [Weckner and Abeyaratne, 2005], [Silling and Bobaru, 2005], [Silling and Lehoucq, 2008], [Silling et al., 2010], [Foster et al., 2011], [Ha and Bobaru, 2010], [Agwai et al., 2011], [Bobaru and Hu, 2012], [Ghajari et al., 2014], [Du et al., 2013a], [Lipton et al., 2016]. The work of [Tian and Du, 2014] provides a framework for analyzing quadrature methods for many linear peridynamics models in the absence of fracture. A recent review of the state of the art can be found in [Bobaru et al., 2016] and [Du, 2018a].

The finite element and finite difference approximations to nonlocal fracture models given in this project are described in chapters two and three. In these chapters we demonstrate that the nonlinear nonlocal fracture models are mathematically well posed and derive the first convergence rates for finite element and finite difference approximations to nonlocal fracture models [Jha and Lipton, 2018a], [Jha and Lipton, 2019a], and [Jha and Lipton, 2019]. The fourth chapter examines the single edge notch specimen in tension and shows theoretically, for the first time [Lipton and Jha, 2019], that the nonlocal fracture evolution converges to the modern dynamic fracture evolution as presented in [Freund, 1998].

1.2 The nonlocal fracture model

We consider a large class of state based peridynamic models where the force at a material point is due to both the strain between two points and the change in volume inside the domain of nonlocal interaction. The pairwise interactions between points are mediated by a

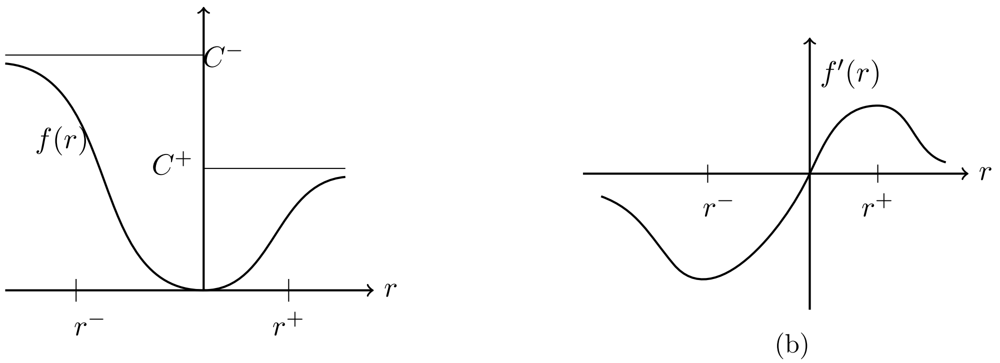

(a)

(b)

Figure 1.1: (a) Potential function $f(r)$ for tensile force. C^+ and C^- are two extreme values of f. (b) Cohesive tensile force.

bond potential of multi-well type while multi point interactions are associated with volume change mediated by a hydrostatic strain potential. The hydrostatic potential can either be a quadratic function, delivering a linear force-strain relation, or a multi-well type that can be associated with material degradation and cavitation. Let $D \subset \mathbb{R}^d$, for $d = 2, 3$, be the material domain. For a displacement field $\boldsymbol{u} : D \times [0, T] \to \mathbb{R}^d$, the strain between two material points $\boldsymbol{x}, \boldsymbol{y} \in D$ is given by

$$S(\boldsymbol{y}, \boldsymbol{x}, t; \boldsymbol{u}) = \frac{\boldsymbol{u}(\boldsymbol{y}, t) - \boldsymbol{u}(\boldsymbol{x}, t)}{|\boldsymbol{y} - \boldsymbol{x}|} \cdot \frac{\boldsymbol{y} - \boldsymbol{x}}{|\boldsymbol{y} - \boldsymbol{x}|}. \tag{1.2.1}$$

Let $\epsilon > 0$ be the size of horizon and $H_\epsilon(\boldsymbol{x}) = \{\boldsymbol{y} \in \mathbb{R}^d : |\boldsymbol{y} - \boldsymbol{x}| < \epsilon\}$ is the neighborhood of a material point $\boldsymbol{x}$. For pairwise interaction, we assume the following form of pairwise interaction potential

$$\mathcal{W}^\epsilon(S(\boldsymbol{y}, \boldsymbol{x}, t; \boldsymbol{u})) = \frac{J^\epsilon(|\boldsymbol{y} - \boldsymbol{x}|)}{\epsilon|\boldsymbol{y} - \boldsymbol{x}|} f(\sqrt{|\boldsymbol{y} - \boldsymbol{x}|} S(\boldsymbol{y}, \boldsymbol{x}, t; \boldsymbol{u})), \tag{1.2.2}$$

where $J^\epsilon(|\boldsymbol{y} - \boldsymbol{x}|)$ is the influence function. We assume $J^\epsilon(|\boldsymbol{y} - \boldsymbol{x}|) = J(|\boldsymbol{y} - \boldsymbol{x}|/\epsilon)$ where $0 \leq J(r) \leq M$ for $r < 1$ and $J(r) = 0$ for $r \geq 1$. The potential f, see Figure 1.1a, is assumed to be convex for small strains and becomes concave for larger strains. In the widely used prototypical micro-elastic brittle (PMB) peridynamic material, the strain vs force profile is linear up to some critical strain S_c and is zero for any strain above S_c. In contrast, the peridynamic force given by $\partial_S \mathcal{W}^\epsilon$, is linear near zero strain and as the strain gets larger and reaches the critical strain, S_c^+ (S_c^-) for positive (negative) strain, the bond starts to soften, see Figure 1.1b. For a given potential function f, the critical strain is given by $S_c^+ = \frac{r^+}{\sqrt{|\boldsymbol{y}-\boldsymbol{x}|}}$ and $S_c^- = \frac{r^-}{\sqrt{|\boldsymbol{y}-\boldsymbol{x}|}}$ where $r^+ > 0, r^- < 0$ are the inflection points of the potential function f as shown in Figure 1.1a.

The spherical or hydrostatic strain $\theta(\boldsymbol{x}, t; \boldsymbol{u})$ at a material point is given by

$$\theta(\boldsymbol{x}, t; \boldsymbol{u}) = \frac{1}{\epsilon^d \omega_d} \int_{H_\epsilon(\boldsymbol{x})} J^\epsilon(|\boldsymbol{y} - \boldsymbol{x}|) S(\boldsymbol{y}, \boldsymbol{x}, t; \boldsymbol{u}) |\boldsymbol{y} - \boldsymbol{x}| \, d\boldsymbol{y}, \tag{1.2.3}$$

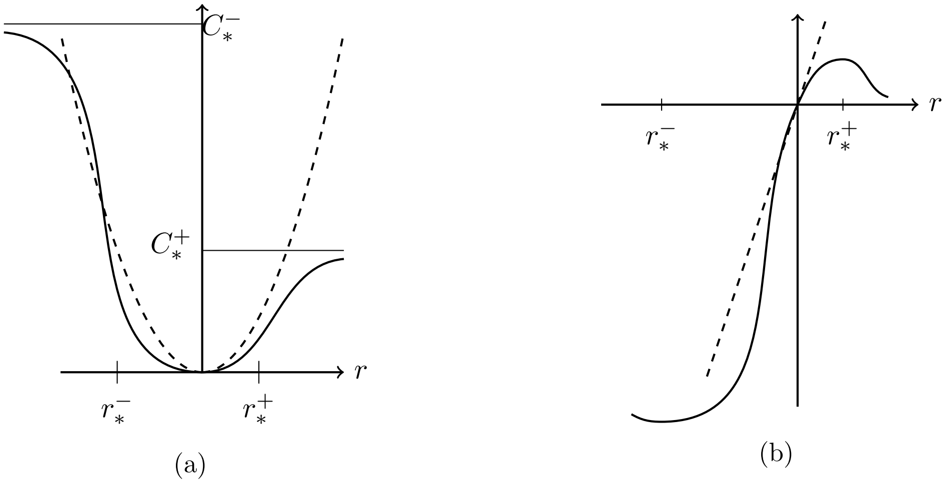

Figure 1.2: (a) Two types of potential function $g(r)$ for hydrostatic force. The dashed line corresponds to the quadratic potential $g(r) = \beta r^2/2$. The solid line corresponds to the convex-concave type potential $g(r)$. For the convex-concave type potential, there are two special points r_*^- and r_*^+ at which material points start to soften. C_*^+ and C_*^- are two extreme values. (b) Hydrostatic forces.

where ω_d is the volume of unit ball in dimension $d = 2, 3$. The potential for hydrostatic interaction is of the form

$$\mathcal{V}^\epsilon(\theta(\boldsymbol{x}, t; \boldsymbol{u})) = \frac{g(\theta(\boldsymbol{x}, t; \boldsymbol{u}))}{\epsilon^2}, \tag{1.2.4}$$

where g is the potential function associated to hydrostatic strain. Here g can be of two types: 1) a quadratic function with only one well at zero strain, and 2) a convex-concave function with a well at the origin and at $\pm\infty$, see Figure 1.2a. If g is assumed to be quadratic then the force due to spherical strain is linear. If g is a multi-well potential, the material softens as the hydrostatic strains exceeds critical value. For the convex-concave type g, the critical values are $0 < \theta_c^+$ and $\theta_c^- < 0$ beyond which the force begins to soften is related to the inflection point r_*^+ and r_*^- of g as follows

$$\theta_c^+ = r_*^+, \qquad \theta_c^- = r_*^-. \tag{1.2.5}$$

The critical compressive hydrostatic strain where the force begins to soften for negative hydrostatic strain is chosen much larger in magnitude than θ_c^+, i.e. $\theta_c^+ << |\theta_c^-|$.

To enforce zero displacement boundary conditions at ∂D and to insure a well posed evolution we introduce the boundary function $\omega(\boldsymbol{x})$. This function is introduced as a factor into the potentials $\mathcal{W}^\epsilon$ and $\mathcal{V}^\epsilon$. Here the boundary function takes value 1 in the interior of domain and is zero on the boundary. We assume $\sup_{\boldsymbol{x}} |\nabla\omega(\boldsymbol{x})| < \infty$ and $\sup_{\boldsymbol{x}} |\nabla^2\omega(\boldsymbol{x})| < \infty$ in our analysis. The hydrostatic strain is modified to include the boundary and is given by

$$\theta(\boldsymbol{x}, t; \boldsymbol{u}) = \frac{1}{\epsilon^d \omega_d} \int_{H_\epsilon(\boldsymbol{x})} \omega(\boldsymbol{y}) J^\epsilon(|\boldsymbol{y} - \boldsymbol{x}|) S(\boldsymbol{y}, \boldsymbol{x}, t; \boldsymbol{u}) |\boldsymbol{y} - \boldsymbol{x}| \, d\boldsymbol{y}. \tag{1.2.6}$$

The peridynamic potentials Equation 1.2.2 and Equation 1.2.4 are modified to *see the* *boundary* as follows

$$\mathcal{W}^\epsilon(S(\boldsymbol{y},\boldsymbol{x},t;\boldsymbol{u})) = \omega(\boldsymbol{x})\omega(\boldsymbol{y})\frac{J^\epsilon(|\boldsymbol{y}-\boldsymbol{x}|)}{\epsilon|\boldsymbol{y}-\boldsymbol{x}|}f(\sqrt{|\boldsymbol{y}-\boldsymbol{x}|}S(\boldsymbol{y},\boldsymbol{x},t;\boldsymbol{u})), \tag{1.2.7}$$

$$\mathcal{V}^\epsilon(\theta(\boldsymbol{x},t;\boldsymbol{u})) = \omega(\boldsymbol{x})\frac{g(\theta(\boldsymbol{x},t;\boldsymbol{u}))}{\epsilon^2}. \tag{1.2.8}$$

We assume that potential function f is at least 4 times differentiable and satisfies following regularity condition:

$$C_0^f := \sup_r |f(r)| < \infty, \qquad C_i^f := \sup_r |f^{(i)}(r)| < \infty, \quad \forall i = 1,2,3,4. \tag{1.2.9}$$

If potential function g is convex-concave type then we assume that g satisfies same regularity condition as f. We denote constants C_i^g, for $i = 0,1,..,4$, similar to C_i^f above.

The total potential energy at time t is given by

$$\begin{aligned} PD^\epsilon(\boldsymbol{u}(t)) = \frac{1}{\epsilon^d\omega_d}\int_D\int_{H_\epsilon(\boldsymbol{x})} |\boldsymbol{y}-\boldsymbol{x}|\mathcal{W}^\epsilon(S(\boldsymbol{y},\boldsymbol{x},t;\boldsymbol{u}))\,d\boldsymbol{y}d\boldsymbol{x} \\ + \int_D \mathcal{V}^\epsilon(\theta(\boldsymbol{x},t;\boldsymbol{u}))\,d\boldsymbol{x}, \end{aligned} \tag{1.2.10}$$

where potential $\mathcal{W}^\epsilon$ and $\mathcal{V}^\epsilon$ are described above. The material is assumed to be homogeneous and the density is given by ρ. The applied body force is denoted by $\boldsymbol{b}(\boldsymbol{x},t)$. We define the Lagrangian

$$\mathrm{L}(\boldsymbol{u},\partial_t\boldsymbol{u},t) = \frac{\rho}{2}||\dot{\boldsymbol{u}}||^2 - PD^\epsilon(\boldsymbol{u}(t)) + \int_D \boldsymbol{b}(t)\cdot\boldsymbol{u}(t)d\boldsymbol{x},$$

here $\dot{\boldsymbol{u}}$ is the velocity given by the time derivative of $\boldsymbol{u}$. Applying the principal of least action gives the nonlocal dynamics

$$\rho\ddot{\boldsymbol{u}}(\boldsymbol{x},t) = \mathcal{L}^\epsilon(\boldsymbol{u})(\boldsymbol{x},t) + \boldsymbol{b}(\boldsymbol{x},t), \text{ for } \boldsymbol{x}\in D, \tag{1.2.11}$$

where

$$\mathcal{L}^\epsilon(\boldsymbol{u})(\boldsymbol{x},t) = \mathcal{L}^\epsilon_T(\boldsymbol{u})(\boldsymbol{x},t) + \mathcal{L}^\epsilon_D(\boldsymbol{u})(\boldsymbol{x},t), \tag{1.2.12}$$

$\mathcal{L}^\epsilon_T(\boldsymbol{u})$ is the peridynamic force due to bond-based interaction and is given by

$$\begin{aligned} &\mathcal{L}^\epsilon_T(\boldsymbol{u})(\boldsymbol{x},t) \\ &= \frac{2}{\epsilon^d\omega_d}\int_{H_\epsilon(\boldsymbol{x})}\omega(\boldsymbol{x})\omega(\boldsymbol{y})\frac{J^\epsilon(|\boldsymbol{y}-\boldsymbol{x}|)}{\epsilon|\boldsymbol{y}-\boldsymbol{x}|}\partial_S f(\sqrt{|\boldsymbol{y}-\boldsymbol{x}|}S(\boldsymbol{y},\boldsymbol{x},t;\boldsymbol{u}))\boldsymbol{e}_{\boldsymbol{y}-\boldsymbol{x}}\,d\boldsymbol{y}, \end{aligned} \tag{1.2.13}$$

and $\mathcal{L}^\epsilon_D(\boldsymbol{u})$ is the peridynamic force due to state-based interaction and is given by

$$\begin{aligned} &\mathcal{L}^\epsilon_D(\boldsymbol{u})(\boldsymbol{x},t) \\ &= \frac{1}{\epsilon^d\omega_d}\int_{H_\epsilon(\boldsymbol{x})}\omega(\boldsymbol{x})\omega(\boldsymbol{y})\frac{J^\epsilon(|\boldsymbol{y}-\boldsymbol{x}|)}{\epsilon^2}\left[\partial_\theta g(\theta(\boldsymbol{y},t;\boldsymbol{u})) + \partial_\theta g(\theta(\boldsymbol{x},t;\boldsymbol{u}))\right]\boldsymbol{e}_{\boldsymbol{y}-\boldsymbol{x}}\,d\boldsymbol{y}. \end{aligned} \tag{1.2.14}$$

The dynamics is complemented with the initial data

$$\boldsymbol{u}(\boldsymbol{x},0) = \boldsymbol{u}_0(\boldsymbol{x}), \qquad \partial_t\boldsymbol{u}(\boldsymbol{x},0) = \boldsymbol{v}_0(\boldsymbol{x}). \tag{1.2.15}$$

We prescribe zero Dirichlet boundary condition on the boundary ∂D

$$\boldsymbol{u}(\boldsymbol{x}) = \boldsymbol{0} \qquad \forall \boldsymbol{x} \in \partial D. \tag{1.2.16}$$

We extend the zero boundary condition outside D to whole $\mathbb{R}^d$.

We conclude with notation that is used throughout. Points and vectors in $\mathbb{R}^d$ are denoted as bold letters. For convenience the key notation is listed here as well as defined where it is first used.

$[0,T]$	Time domain
ϵ	Size of horizon
ρ	Density
$H_\epsilon(\boldsymbol{x})$	Horizon of $\boldsymbol{x} \in D$, a ball of radius ϵ centered at $\boldsymbol{x}$
ω_d	Volume of unit ball in dimension $d = 2, 3$
$\omega(\boldsymbol{x}) \in [0,1]$	Boundary function defined on D taking value 1 in the interior and smoothly decaying to 0 as $\boldsymbol{x}$ approaches ∂D
$\boldsymbol{u}$	Displacement field defined over $D \times [0,T]$. We may also use notation $\boldsymbol{u}$ to denote field defined over just D
$\boldsymbol{u}_0, \boldsymbol{v}_0$	Initial condition on displacement
$\boldsymbol{b}$	Body force defined over $D \times [0,T]$
$\boldsymbol{e}_{\boldsymbol{y}-\boldsymbol{x}}$	The unit vector pointing from a point $\boldsymbol{y}$ to the point $\boldsymbol{x}$
$S = S(\boldsymbol{y}, \boldsymbol{x}, t; \boldsymbol{u})$	Bond strain $S = \frac{\boldsymbol{u}(\boldsymbol{y},t)-\boldsymbol{u}(\boldsymbol{x},t)}{\lvert\boldsymbol{y}-\boldsymbol{x}\rvert} \cdot \boldsymbol{e}_{\boldsymbol{y}-\boldsymbol{x}}$. We may also use $S(\boldsymbol{y}, \boldsymbol{x}; \boldsymbol{u})$ if $\boldsymbol{u}$ is a filed defined over just D
$\theta = \theta(\boldsymbol{x}, t; \boldsymbol{u})$	Spherical or hydrostatic strain. We may also use $\theta(\boldsymbol{x}; \boldsymbol{u})$ if $\boldsymbol{u}$ is a filed defined over just D
S_c^+, S_c^-	Critical bond strain
θ_c^+, θ_c^-	Critical hydrostatic strain
$J^\epsilon(r) = J(r/\epsilon)$	Influence function where J is integrable with $J(r) = 0$ for $r \geq 1$ and $0 \leq J(r) \leq M$ for $r < 1$
$\bar{J}_\alpha$	Moment of function J over $H_1(\boldsymbol{0})$ with weight $1/(\omega_d \lvert\boldsymbol{\xi}\rvert^\alpha)$
f, g	Potential functions for pairwise and state-based interaction
$\mathcal{W}^\epsilon, \mathcal{V}^\epsilon$	Pairwise and state-based potential energy density
$PD^\epsilon(\boldsymbol{u}(t))$	Total peridynamic potential energy at time t
$\mathcal{E}^\epsilon(\boldsymbol{u})(t)$	Total dynamic energy at time t
$\mathcal{L}^\epsilon, \mathcal{L}_T^\epsilon, \mathcal{L}_D^\epsilon$	total peridynamic force, pairwise peridynamic force, and state-based peridynamic force respectively
$a^\epsilon(\boldsymbol{u}, \boldsymbol{v})$	Nonlinear operator where $\boldsymbol{u}, \boldsymbol{v}$ are vector fields over D
$a_T^\epsilon, a_D^\epsilon$	Nonlinear pairwise and state-based operator
$\lvert\lvert \cdot \rvert\rvert, \lvert\lvert \cdot \rvert\rvert_\infty, \lvert\lvert \cdot \rvert\rvert_n$	L^2 norm over D, L^∞ norm over D, and Sobolev H^n norm over D (for $n = 1, 2$) respectively

$h, \Delta t$	Size of mesh and size of time step
$\mathcal{T}_h$	Triangulation of D given by triangular/tetrahedral elements
$\mathcal{I}_h$	Continuous piecewise linear interpolation operator on $\mathcal{T}_h$
W	Space of functions in $H^2(D;\mathbb{R}^d)$ such that trace of function is zero on boundary ∂D, i.e. $W = H^2(D;\mathbb{R}^d) \cap H^1_0(D;\mathbb{R}^d)$
V_h	Space of continuous piecewise linear interpolations on $\mathcal{T}_h$
ϕ_i	Interpolation function of mesh node i
$\boldsymbol{r}_h(\boldsymbol{u})$	Finite element projection of $\boldsymbol{u}$ onto V_h
E^k	Total error in mean square norm at time step k
$\boldsymbol{u}^k_h, \boldsymbol{v}^k_h$	Approximate displacement and velocity field at time step k
$\boldsymbol{u}^k, \boldsymbol{v}^k$	Exact displacement and velocity field at time step k

Chapter 2

Finite element approximation of nonlocal fracture models

2.1 Introduction

In this chapter we focus on finite element approximations. We first show the well-posedness of the peridynamic formulation and that peridynamic evolutions exist in the Sobolev space H^2. Application of earlier work [Lipton, 2016], [Lipton, 2014] shows that these solutions converge as the nonlocal interaction goes to zero, in mean square, to sharp fracture solutions where evolving cracks are growing in otherwise elastic regions. The finite element approximation has been applied to peridynamic fracture, however to the best of the PI's knowledge this investigation is the first to develop rigorous a-priori convergence theory for the finite element approximation to peridynamic problems in the presence of material failure. In this project we first prove existence of peridynamic evolutions taking values in $H^2(D;\mathbb{R}^d) \cap H_0^1(D;\mathbb{R}^d)$ that are twice differentiable in time, see Theorem 2.1.2. We note that as these evolutions will become more fracture like as the region of nonlocal interaction decreases. These evolutions can be thought of as inner approximations (or regularized) fracture evolutions. On passing to subsequences it is possible to show that the $H^2(D;\mathbb{R}^d) \cap H_0^1(D;\mathbb{R}^d)$ evolutions converge in the limit of vanishing non-locality to a limit solution taking values in the space of special functions of bounded deformation SBD. Functions in the class SBD have localized jump sets and off these sets they have well defined gradients. This is the function space used for fracture. Here the limit evolution has a well defined Griffith fracture energy bounded by the initial data, see [Lipton, 2016] and [Jha and Lipton, 2019b]. We show here that higher temporal regularity can be established if the body force changes smoothly in time. Motivated by these considerations we develop finite element error estimates for solutions that take values in $H^2(D;\mathbb{R}^d) \cap H_0^1(D;\mathbb{R}^d)$ and for a bounded time interval.

In this project we obtain an a-priori L^2 error bound for the finite element approximation of the displacement and velocity using a central in time discretization. Due to the nonlinear nature of the problem we get a convergence rate by using Lax Richtmyer stability together with consistency. Both stability and consistency are shown to follow from the Lipschitz continuity of the peridynamic force in $L^2(D;\mathbb{R}^d)$. We show that the finite element approximations converge to the H^2 solutions uniformly in time as measured in the mean square norm. For linear continuous finite elements the convergence rate is shown to be

$C_t\Delta t + C_s h^2/\epsilon^2$, where ϵ is the size of horizon, h is the mesh size, and Δt is the size of time step. The constants C_t and C_s are independent of Δt and h and may depend on ϵ through the norm of the exact solution, see Theorem 3.3.3. We demonstrate the stability of the semi-discrete approximation. The stability of the fully discrete approximation is shown for the linearized peridynamic force. We will present numerical simulations with dynamic crack propagation that support the theoretical convergence rate. A more elaborate discussion of the a-priori bound is presented in section subsection 2.3.2. For the linearized model we obtain a stability condition on Δt, Theorem 2.3.2, that is of the same form as those given for linear local and nonlocal wave equations [Karaa, 2012, Guan and Gunzburger, 2015]. We demonstrate stability for the linearized model noting that for small strains the material behaves like a linear elastic material and that the stability of the linearized model is necessary for the stability of the nonlinear model. We believe a more constructive CFL stability condition is possible for the linear case and will pursue this in future work.

We carry out numerical experiments for dynamic crack propagation and obtain convergence rates for Plexiglass that are in line with the theory, see section 2.4. We also compare the Griffith's fracture energy with the peridynamic energy of the material softening zone we show good agreement between the two energies, see subsection 2.4.2. Finite difference methods are less expensive than finite element approximations for nonlocal problems, however the latter offers more control on the accuracy of solution see, [Macek and Silling, 2007, Littlewood, 2010, Du et al., 2013c, Gerstle et al., 2007, Du, 2018b].

Here the a-priori L^2 convergence rates for the FEM given by Theorem 3.3.3 include the effects of material degradation through the softening of material properties. The FEM simulations presented in this paper show that the material develops localized softening zones (region where bonds exceed critical tensile strain) as it deforms. This is in contrast to linear peridynamic models which are incapable of developing softening zones. For nonlinear peridynamic models with material failure the localization of zones of softening and damage is the hallmark of peridynamic modeling [Silling, 2000, Silling et al., 2007], [Ha and Bobaru, 2010], [Foster et al., 2011]. One notes that the a-priori error involves ϵ in the denominator and in many cases ϵ is chosen small. However typical dynamic fracture experiments last only hundreds of microseconds and the a-priori error is controlled by the product of simulation time multiplied by h^2/ϵ^2. So for material properties characteristic of Plexiglass and ϵ of size $4mm$, the a-priori estimates predict a relative error of 1/10 for simulations lasting around 100 microseconds. We point out that the a-priori error estimates assume the appearance of nonlinearity anywhere in the computational domain. On the other hand numerical simulation and independent theoretical estimates show that the nonlinearity concentrates along cracks of finite length and width equal to ϵ, see [Lipton, 2016, Lipton, 2014]. Moreover the remainder of the computational domain is seen to behave linearly and to leading order can be modeled as a linear elastic material up to an error proportional to ϵ, see [Proposition 6, [Jha and Lipton 2018b]]. Future work will use these observations to focus on adaptive implementation and a-posteriori estimates. A-posteriori convergence for FEM models of peridynamics with material degradation can be seen in the work [Macek and Silling, 2007], [Chen and Gunzburger, 2011], [Ren et al., 2017]. For other nonlinear and nonlocal models adaptive mesh refinement within FE framework for nonlocal models has been explored in [Du et al., 2013c] and convergence of the adaptive FE approximation is rigorously shown. A-posteriori error analysis of linear nonlocal models is carried out in [Du et al., 2013b].

2.1.1 Existence of solutions and higher regularity in time

We recall that the space $H_0^n(D;\mathbb{R}^d)$ is the closure in the H^n norm of the functions that are infinitely differentiable with compact support in D. For suitable initial conditions and body force we have shown that solutions exist in

$$W = H^2(D;\mathbb{R}^d) \cap H_0^1(D;\mathbb{R}^d) = \{v \in H^2(D;\mathbb{R}^d) : \gamma v = 0, \text{ on } \partial D\} \tag{2.1.1}$$

where γ is the trace of the function v on the boundary of D. We will assume that $\boldsymbol{u} \in W$ is extended by zero outside D. We first exhibit the Lipschitz continuity property and boundedness of the peridynamic force for displacements in W. We then apply [Theorem 3.2, [Jha and Lipton, 2019]] to conclude the existence of unique solutions.

The Lipschitz continuity property of a peridynamic force $\mathcal{L}^\epsilon$.

Theorem 2.1.1 ***Lipschitz continuity of peridynamic force***
Let f be a convex-concave function satisfying $C_i^f < \infty$ for $i = 0,..,4$ and let g either be a quadratic function, or g be a convex-concave function with $C_i^g < \infty$ for $i = 0,..,4$. Also, let boundary function $\omega : D \to [0,1]$ be such that $\sup_{\boldsymbol{x}\in D} |\nabla\omega(\boldsymbol{x})| < \infty$ and $\sup_{\boldsymbol{x}\in D} |\nabla^2\omega(\boldsymbol{x})| < \infty$. Then, for any $\boldsymbol{u}, \boldsymbol{v} \in W$, we have

$$||\mathcal{L}^\epsilon(\boldsymbol{u}) - \mathcal{L}^\epsilon(\boldsymbol{v})||_2 \leq \frac{\bar{L}_1(1 + ||\boldsymbol{u}||_2 + ||\boldsymbol{v}||_2)^2}{\epsilon^3}||\boldsymbol{u} - \boldsymbol{v}||_2, \tag{2.1.2}$$

where constant $\bar{L}_1$ does not depend on ϵ and $\boldsymbol{u}, \boldsymbol{v}$. Also, for $\boldsymbol{u} \in W$, we have

$$||\mathcal{L}^\epsilon(\boldsymbol{u})||_2 \leq \frac{\bar{L}_2(||\boldsymbol{u}||_2 + ||\boldsymbol{u}||_2^2)}{\epsilon^{5/2}}, \tag{2.1.3}$$

where constant $\bar{L}_2$ does not depend on ϵ and $\boldsymbol{u}$.

Now let $T > 0$ be any positive number, a straight-forward application of [Theorem 3.2, [Jha and Lipton, 2019]] gives:

Theorem 2.1.2 ***Existence and uniqueness of solutions over finite time intervals***
Let f, g, and ω satisfy the hypothesis of Theorem 2.1.1. For any initial condition $\boldsymbol{u}_0, \boldsymbol{v}_0 \in W$, time interval $I_0 = (-T, T)$, and right hand side $\boldsymbol{b}(t)$ continuous in time for $t \in I_0$ such that $\boldsymbol{b}(t)$ satisfies $\sup_{t\in I_0} ||\boldsymbol{b}(t)||_2 < \infty$, there is a unique solution $\boldsymbol{u}(t) \in C^2(I_0; W)$ of peridynamic equation 1.2.11. Also, $\boldsymbol{u}(t)$ and $\dot{\boldsymbol{u}}(t)$ are Lipschitz continuous in time for $t \in I_0$.

We also have shown higher regularity in time of the evolutions:

Theorem 2.1.3 ***Higher regularity***
Suppose the initial data and righthand side $\boldsymbol{b}(t)$ satisfy the hypothesis of Theorem 2.1.2 and suppose further that $\dot{\boldsymbol{b}}(t)$ exists and is continuous in time for $t \in I_0$ and $\sup_{t\in I_0} ||\dot{\boldsymbol{b}}(t)||_2 < \infty$. Then $\boldsymbol{u} \in C^3(I_0; W)$ and

$$||\partial^3_{ttt}\boldsymbol{u}(\boldsymbol{x}, t)||_2 \leq \frac{C(1 + \sup_{s\in I_0} ||\boldsymbol{u}(s)||_2)^2}{\epsilon^3} \sup_{s\in I_0} ||\partial_t \boldsymbol{u}(s)||_2 + ||\dot{\boldsymbol{b}}(\boldsymbol{x}, t)||_2, \tag{2.1.4}$$

where C is a positive constant independent of $\boldsymbol{u}$.

We also can conclude Lipshitz continuity of the peridynamic force in the L^2 (mean square) norm. For any $\boldsymbol{u}, \boldsymbol{v} \in L^2_0(D; \mathbb{R}^d)$, we have with respect to

$$||\mathcal{L}^\epsilon(\boldsymbol{u}) - \mathcal{L}^\epsilon(\boldsymbol{v})|| \leq \frac{L}{\epsilon^2} ||\boldsymbol{u} - \boldsymbol{v}||. \tag{2.1.5}$$

where we have an explicit formula for the constant L is given by

$$L := \begin{cases} 4(C^f_2 \bar{J}_1 + C^g_2 \bar{J}^2_0) & \text{if } g \text{ is a convex-concave type,} \\ 4(C^f_2 \bar{J}_1 + g''(0) \bar{J}^2_0) & \text{if } g \text{ is a quadratic function,} \end{cases} \tag{2.1.6}$$

and $\bar{J}^\alpha = (1/\omega_d) \int_{H_1(\mathbf{0})} J(|\boldsymbol{\xi}|)/|\boldsymbol{\xi}|^\alpha d\boldsymbol{\xi}$.

2.1.2 Weak form

We multiply Equation 1.2.11 by a test function $\tilde{\boldsymbol{u}}$ in $H^1_0(D; \mathbb{R}^d)$ and integrate over D to get

$$(\ddot{\boldsymbol{u}}(t), \tilde{\boldsymbol{u}}) = (\mathcal{L}^\epsilon(\boldsymbol{u}(t)), \tilde{\boldsymbol{u}}) + (\boldsymbol{b}(t), \tilde{\boldsymbol{u}}). \tag{2.1.7}$$

We have the following integration by parts formula:

Lemma 2.1.4 *For any $\boldsymbol{u}, \boldsymbol{v} \in L^2_0(D; \mathbb{R}^d)$ we have*

$$(\mathcal{L}^\epsilon(\boldsymbol{u}), \boldsymbol{v}) = -a^\epsilon(\boldsymbol{u}, \boldsymbol{v}), \tag{2.1.8}$$

where

$$a^\epsilon(\boldsymbol{u}, \boldsymbol{v}) = a^\epsilon_T(\boldsymbol{u}, \boldsymbol{v}) + a^\epsilon_D(\boldsymbol{u}, \boldsymbol{v}) \tag{2.1.9}$$

and

$$\begin{aligned} a^\epsilon_T(\boldsymbol{u}, \boldsymbol{v}) = \frac{1}{\epsilon^{d+1} \omega_d} \int_D \int_D & \omega(\boldsymbol{x}) \omega(\boldsymbol{y}) J^\epsilon(|\boldsymbol{y} - \boldsymbol{x}|) \\ & \partial_S f(\sqrt{|\boldsymbol{y} - \boldsymbol{x}|} S(\boldsymbol{y}, \boldsymbol{x}; \boldsymbol{u})) S(\boldsymbol{y}, \boldsymbol{x}; \boldsymbol{v}) d\boldsymbol{y} d\boldsymbol{x}, \\ a^\epsilon_D(\boldsymbol{u}, \boldsymbol{v}) = \frac{1}{\epsilon^2} \int_D & \omega(\boldsymbol{x}) g'(\theta(\boldsymbol{x}; \boldsymbol{u})) \theta(\boldsymbol{x}; \boldsymbol{v}) d\boldsymbol{x}. \end{aligned} \tag{2.1.10}$$

The proof of above lemma is identical to the proof of Lemma 4.2 in [Lipton et al., 2018a].

Using the above Lemma, the weak form of the peridynamic evolution is given by

$$(\ddot{\boldsymbol{u}}(t), \tilde{\boldsymbol{u}}) + a^\epsilon(\boldsymbol{u}(t), \tilde{\boldsymbol{u}}) = (\boldsymbol{b}(t), \tilde{\boldsymbol{u}}). \tag{2.1.11}$$

Total dynamic energy: We define the total dynamic energy as follows

$$\mathcal{E}^\epsilon(\boldsymbol{u})(t) = \frac{1}{2} ||\dot{\boldsymbol{u}}(t)||^2_{L^2} + PD^\epsilon(\boldsymbol{u}(t)), \tag{2.1.12}$$

where PD^ϵ is defined in Equation 1.2.10. Time derivative of total energy satisfies

$$\frac{d}{dt} \mathcal{E}^\epsilon(\boldsymbol{u})(t) = (\ddot{\boldsymbol{u}}(t), \dot{\boldsymbol{u}}(t)) + a^\epsilon(\boldsymbol{u}(t), \dot{\boldsymbol{u}}(t)). \tag{2.1.13}$$

Remark. It is readily verified that the peridynamic force and energy are bounded for all functions in $L^2(D;\mathbb{R}^d)$. Here the bound on the force follows from the Lipschitz property of the force in $L^2(D;\mathbb{R}^d)$, see, Equation 2.1.5. The peridynamic force is also bounded for functions $\boldsymbol{u}$ in $H^1(D;\mathbb{R}^d)$. This again follows from the Lipschitz property of the force in $H^1(D;\mathbb{R}^d)$. The boundedness of the energy $PD^\epsilon(\boldsymbol{u})$ in both $L^2(D;\mathbb{R}^d)$ and $H^1(D;\mathbb{R}^d)$ follows from the boundedness of the bond potential energy $\mathcal{W}^\epsilon(S(\boldsymbol{y},\boldsymbol{x},t;\boldsymbol{u}))$ and $\mathcal{V}^\epsilon(\theta(\boldsymbol{x},t;\boldsymbol{u}))$ used in the definition of $PD^\epsilon(\boldsymbol{u})$, see Equation 1.2.7 and Equation 1.2.8. More generally this also shows that $PD^\epsilon(\boldsymbol{u}) < \infty$ for $\boldsymbol{u} \in L^1(D;\mathbb{R}^d)$.

We next discuss the spatial and the time discretization of peridynamic equation.

2.2 Finite element approximation

Let V_h be given by linear continuous interpolations over tetrahedral or triangular elements $\mathcal{T}_h$ where h denotes the size of finite element mesh. Here we assume the elements are conforming and the finite element mesh is shape regular and $V_h \subset H^1_0(D;\mathbb{R}^d)$.

For a continuous function $\boldsymbol{u}$ on $\bar{D}$, $\mathcal{I}_h(\boldsymbol{u})$ is the continuous piecewise linear interpolant on $\mathcal{T}_h$. It is given by

$$\mathcal{I}_h(\boldsymbol{u})\bigg|_T = \mathcal{I}_T(\boldsymbol{u}) \qquad \forall T \in \mathcal{T}_h, \tag{2.2.1}$$

where $\mathcal{I}_T(\boldsymbol{u})$ is the local interpolant defined over finite element T and is given by

$$\mathcal{I}_T(\boldsymbol{u}) = \sum_{i=1}^{n} \boldsymbol{u}(\boldsymbol{x}_i)\phi_i. \tag{2.2.2}$$

Here n is the number of vertices in an element T, $\boldsymbol{x}_i$ is the position of vertex i, and ϕ_i is the linear interpolant associated to vertex i.

Application of Theorem 4.4.20 and remark 4.4.27 in [Brenner and Scott, 2007] gives

$$||\boldsymbol{u} - \mathcal{I}_h(\boldsymbol{u})|| \leq ch^2||\boldsymbol{u}||_2, \qquad \forall \boldsymbol{u} \in W. \tag{2.2.3}$$

Let $\boldsymbol{r}_h(\boldsymbol{u})$ denote the projection of $\boldsymbol{u} \in W$ on V_h. For the L^2 norm it is defined as

$$||\boldsymbol{u} - \boldsymbol{r}_h(\boldsymbol{u})|| = \inf_{\tilde{\boldsymbol{u}} \in V_h} ||\boldsymbol{u} - \tilde{\boldsymbol{u}}||. \tag{2.2.4}$$

and satisfies

$$(\boldsymbol{r}_h(\boldsymbol{u}), \tilde{\boldsymbol{u}}) = (\boldsymbol{u}, \tilde{\boldsymbol{u}}), \qquad \forall \tilde{\boldsymbol{u}} \in V_h. \tag{2.2.5}$$

Since $\mathcal{I}_h(\boldsymbol{u}) \in V_h$, and Equation 2.2.3 we see that

$$||\boldsymbol{u} - \boldsymbol{r}_h(\boldsymbol{u})|| \leq ch^2||\boldsymbol{u}||_2, \qquad \forall \boldsymbol{u} \in W \tag{2.2.6}$$

2.2.1 Semi-discrete approximation

Let $\boldsymbol{u}_h(t) \in V_h$ be the approximation of $\boldsymbol{u}(t)$ satisfying following for all $t \in [0,T]$

$$(\ddot{\boldsymbol{u}}_h, \tilde{\boldsymbol{u}}) + a^\epsilon(\boldsymbol{u}_h(t), \tilde{\boldsymbol{u}}) = (\boldsymbol{b}(t), \tilde{\boldsymbol{u}}), \qquad \forall \tilde{\boldsymbol{u}} \in V_h. \tag{2.2.7}$$

We have following result:

Theorem 2.2.1 ***Energy stability of semi-discrete approximation***
The semi-discrete scheme is stable and the energy $\mathcal{E}^\epsilon(\boldsymbol{u}_h)(t)$, defined in Equation 2.1.12, satisfies the following bound

$$\mathcal{E}^\epsilon(\boldsymbol{u}_h)(t) \leq \left[\sqrt{\mathcal{E}^\epsilon(\boldsymbol{u}_h)(0)} + \int_0^t ||\boldsymbol{b}(\tau)|| d\tau\right]^2 .$$

2.3 Central difference time discretization

In subsection 2.3.2 we calculate the convergence rate for the central difference time discretization of the fully nonlinear problem. We then present a CFL like condition on the time step Δt for the linearized peridynamic equation in subsection 2.3.3.

At time step k, the exact solution is given by $(\boldsymbol{u}^k, \boldsymbol{v}^k)$ where $\boldsymbol{v}^k = \partial \boldsymbol{u}^k/\partial t$, and their projection onto V_h is given by $(\boldsymbol{r}_h(\boldsymbol{u}^k), \boldsymbol{r}_h(\boldsymbol{v}^k))$. The solution of fully discrete problem at time step k is given by $(\boldsymbol{u}^k_h, \boldsymbol{v}^k_h)$.

We approximate the initial data on displacement $\boldsymbol{u}_0$ and velocity $\boldsymbol{v}_0$ by their projections $\boldsymbol{r}_h(\boldsymbol{u}_0)$ and $\boldsymbol{r}_h(\boldsymbol{v}_0)$. Let $\boldsymbol{u}^0_h = \boldsymbol{r}_h(\boldsymbol{u}_0)$ and $\boldsymbol{v}^0_h = \boldsymbol{r}_h(\boldsymbol{v}_0)$. For $k \geq 1$, $(\boldsymbol{u}^k_h, \boldsymbol{v}^k_h)$ satisfies, for all $\tilde{\boldsymbol{u}} \in V_h$,

$$\begin{aligned} \left(\frac{\boldsymbol{u}^{k+1}_h - \boldsymbol{u}^k_h}{\Delta t}, \tilde{\boldsymbol{u}}\right) &= (\boldsymbol{v}^{k+1}_h, \tilde{\boldsymbol{u}}), \\ \left(\frac{\boldsymbol{v}^{k+1}_h - \boldsymbol{v}^k_h}{\Delta t}, \tilde{\boldsymbol{u}}\right) &= (\mathcal{L}^\epsilon(\boldsymbol{u}^k_h), \tilde{\boldsymbol{u}}) + (\boldsymbol{b}^k_h, \tilde{\boldsymbol{u}}), \end{aligned} \tag{2.3.1}$$

where we have denoted the projection of $\boldsymbol{b}(t^k)$, i.e. $\boldsymbol{r}_h(\boldsymbol{b}(t^k))$, as $\boldsymbol{b}^k_h$. Combining the two equations delivers central difference equation for $\boldsymbol{u}^k_h$. We have

$$\left(\frac{\boldsymbol{u}^{k+1}_h - 2\boldsymbol{u}^k_h + \boldsymbol{u}^{k-1}_h}{\Delta t^2}, \tilde{\boldsymbol{u}}\right) = (\mathcal{L}^\epsilon(\boldsymbol{u}^k_h), \tilde{\boldsymbol{u}}) + (\boldsymbol{b}^k_h, \tilde{\boldsymbol{u}}), \qquad \forall \tilde{\boldsymbol{u}} \in V_h. \tag{2.3.2}$$

For $k = 0$, we have $\forall \tilde{\boldsymbol{u}} \in V_h$

$$\left(\frac{\boldsymbol{u}^1_h - \boldsymbol{u}^0_h}{\Delta t^2}, \tilde{\boldsymbol{u}}\right) = \frac{1}{2}(\mathcal{L}^\epsilon(\boldsymbol{u}^0_h), \tilde{\boldsymbol{u}}) + \frac{1}{\Delta t}(\boldsymbol{v}^0_h, \tilde{\boldsymbol{u}}) + \frac{1}{2}(\boldsymbol{b}^0_h, \tilde{\boldsymbol{u}}). \tag{2.3.3}$$

2.3.1 Implementation details

For completeness we describe the implementation of the time stepping method using FEM interpolants. Let $\boldsymbol{N}$ be the shape tensor then $\boldsymbol{u}^k_h, \tilde{\boldsymbol{u}} \in V_h$ are given by

$$\boldsymbol{u}^k_h = \boldsymbol{N}\boldsymbol{U}^k, \qquad \tilde{\boldsymbol{u}} = \boldsymbol{N}\tilde{\boldsymbol{U}}, \tag{2.3.4}$$

where $\boldsymbol{U}^k$ and $\tilde{\boldsymbol{U}}$ are Nd dimensional vectors, where N is the number of nodal points in the mesh and d is the dimension.

From Equation 2.3.2, for all $\tilde{\boldsymbol{U}} \in \mathbb{R}^{Nd}$ with elements of $\tilde{\boldsymbol{U}}$ zero on the boundary, then the following holds for $k \geq 1$

$$\left[\boldsymbol{M} \frac{\boldsymbol{U}^{k+1} - 2\boldsymbol{U}^k + \boldsymbol{U}^{k-1}}{\Delta t^2} \right] \cdot \tilde{\boldsymbol{U}} = \boldsymbol{F}^k \cdot \tilde{\boldsymbol{U}}. \tag{2.3.5}$$

Here the mass matrix $\boldsymbol{M}$ and force vector $\boldsymbol{F}^k$ are given by

$$\begin{aligned} \boldsymbol{M} &:= \int_D \boldsymbol{N}^T \boldsymbol{N} d\boldsymbol{x}, \\ \boldsymbol{F}^k &:= \boldsymbol{F}^k_{pd} + \int_D \boldsymbol{N}^T \boldsymbol{b}(\boldsymbol{x}, t^k) d\boldsymbol{x}, \end{aligned} \tag{2.3.6}$$

where $\boldsymbol{F}^k_{pd}$ is defined by

$$\boldsymbol{F}^k_{pd} := \int_D \boldsymbol{N}^T (\mathcal{L}^\epsilon(\boldsymbol{u}^k_h)(\boldsymbol{x})) d\boldsymbol{x}. \tag{2.3.7}$$

We remark that a similar equation holds for $k = 0$.

At the time step k we must invert $\boldsymbol{M}$ to solve for $\boldsymbol{U}^{k+1}$ using

$$\boldsymbol{U}^{k+1} = \Delta t^2 \boldsymbol{M}^{-1} \boldsymbol{F}^k + 2\boldsymbol{U}^k - \boldsymbol{U}^{k-1}. \tag{2.3.8}$$

As is well known this inversion amounts to an increase of computational complexity associated with discrete approximation of the weak formulation of the evolution. Further, the matrix-vector multiplication $\boldsymbol{M}^{-1}\boldsymbol{F}^k$ needs to be carried out at each time step. On the other hand the quadrature error in the computation of the force vector $\boldsymbol{F}^k_{pd}$ is reduced when using the weak form.

We next show the convergence of approximation.

2.3.2 Convergence of approximation

In this section, we prove the uniform bound on the error and show that the approximate solution converges to the exact solution with rate given by $C_t \Delta t + C_s h^2/\epsilon^2$. Here horizon $\epsilon > 0$ is assumed to be fixed. We first compare the exact solution with its projection in V_h and then compare the projection with the approximate solution. We further divide the calculation of error between the projection and the approximate solution in two parts, namely consistency analysis and error analysis.

Error E^k is given by

$$E^k := ||\boldsymbol{u}^k_h - \boldsymbol{u}(t^k)|| + ||\boldsymbol{v}^k_h - \boldsymbol{v}(t^k)||.$$

The error is split into two parts as follows

$$E^k \leq \Big(||\boldsymbol{u}^k - \boldsymbol{r}_h(\boldsymbol{u}^k)|| + ||\boldsymbol{v}^k - \boldsymbol{r}_h(\boldsymbol{v}^k)|| \Big) + \Big(||\boldsymbol{r}_h(\boldsymbol{u}^k) - \boldsymbol{u}^k_h|| + ||\boldsymbol{r}_h(\boldsymbol{v}^k) - \boldsymbol{v}^k_h|| \Big),$$

where the first term is the error between the exact solution and projection, and the second term is the error between the projection and approximate solution. Let

$$\boldsymbol{e}^k_h(\boldsymbol{u}) := \boldsymbol{r}_h(\boldsymbol{u}^k) - \boldsymbol{u}^k_h \quad \text{and} \quad \boldsymbol{e}^k_h(\boldsymbol{v}) := \boldsymbol{r}_h(v^k) - \boldsymbol{v}^k_h \tag{2.3.9}$$

and

$$e^k := ||\boldsymbol{e}_h^k(\boldsymbol{u})|| + ||\boldsymbol{e}_h^k(\boldsymbol{v})||. \tag{2.3.10}$$

Using Equation 2.2.6, we have

$$E^k \leq C_p h^2 + e^k, \tag{2.3.11}$$

where

$$C_p := c\left[\sup_t ||\boldsymbol{u}(t)||_2 + \sup_t ||\frac{\partial \boldsymbol{u}(t)}{\partial t}||_2\right]. \tag{2.3.12}$$

We have the following a-priori convergence rate given by

Theorem 2.3.1 ***Convergence of Central difference approximation***
Let $(\boldsymbol{u}, \boldsymbol{v})$ be the exact solution of the peridynamic equation 1.2.11. Let $(\boldsymbol{u}_h^k, \boldsymbol{v}_h^k)$ be the FE solution of Equation 2.3.1. If $\boldsymbol{u}, \boldsymbol{v} \in C^2([0,T]; W)$, then the scheme is consistent and the error E^k satisfies following bound

$$\begin{aligned}&\sup_{k\leq T/\Delta t} E^k \\ &= C_p h^2 + \exp[T(1 + L/\epsilon^2)(\frac{1}{1-\Delta t})]\left[e^0 + \left(\frac{T}{1-\Delta t}\right)\left(C_t\Delta t + C_s\frac{h^2}{\epsilon^2}\right)\right]\end{aligned} \tag{2.3.13}$$

where the constants C_p, C_t, and C_s are given by Equation 2.3.12. The constant L/ϵ^2 is the Lipschitz constant of the peridynamic force $\mathcal{L}^\epsilon(\boldsymbol{u})$ in L^2, see Equation 2.1.5. If the error in initial data is zero then E^k is of the order of $C_t\Delta t + C_s h^2/\epsilon^2$.

In Theorem 2.1.3 we have shown that $\boldsymbol{u}, \boldsymbol{v} \in C^2([0,T]; W)$ for righthand side $\boldsymbol{b} \in C^1([0,T]; W)$. In section 2.5 we discuss the behavior of the exponential constant appearing in Theorem 3.3.3 for evolution times seen in fracture experiments.

2.3.3 Linearized peridynamics and energy stability

In this section, we linearize the peridynamics model and state a CFL like stability condition. For problems where strains are small, the stability condition for the linearized model is expected to apply to the nonlinear model. The slope of peridynamics potential f and g are constant for sufficiently small strain and therefore for small strain the nonlinear model behaves like a linear model.

In Equation 1.2.13, linearization gives

$$\mathcal{L}_{T,l}^\epsilon(\boldsymbol{u})(\boldsymbol{x}) = \frac{2}{\epsilon^{d+1}\omega_d}\int_{H_\epsilon(\boldsymbol{x})} \omega(\boldsymbol{x})\omega(\boldsymbol{y})J^\epsilon(|\boldsymbol{y}-\boldsymbol{x}|)f''(0)S(\boldsymbol{y},\boldsymbol{x};\boldsymbol{u})\boldsymbol{e}_{\boldsymbol{y}-\boldsymbol{x}}d\boldsymbol{y}. \tag{2.3.14}$$

The corresponding bilinear form is denoted as $a_{T,l}^\epsilon$ and is given by

$$a_{T,l}^\epsilon(\boldsymbol{u},\boldsymbol{v}) = \frac{f''(0)}{\epsilon^{d+1}\omega_d}\int_D\int_D \omega(\boldsymbol{x})\omega(\boldsymbol{y})J^\epsilon(|\boldsymbol{y}-\boldsymbol{x}|)|\boldsymbol{y}-\boldsymbol{x}|S(\boldsymbol{y},\boldsymbol{x};\boldsymbol{u})S(\boldsymbol{y},\boldsymbol{x};\boldsymbol{v})d\boldsymbol{y}d\boldsymbol{x}. \tag{2.3.15}$$

Similarly, linearization of $\mathcal{L}^\epsilon_D$ in Equation 1.2.14 gives

$$\mathcal{L}^\epsilon_{D,l}(\boldsymbol{u})(\boldsymbol{x}) = \frac{g''(0)}{\epsilon^{d+2}\omega_d}\int_{H_\epsilon(\boldsymbol{x})}\omega(\boldsymbol{x})\omega(\boldsymbol{y})J^\epsilon(|\boldsymbol{y}-\boldsymbol{x}|)\left[\theta(\boldsymbol{y},t;\boldsymbol{u})+\theta(\boldsymbol{x},t;\boldsymbol{u})\right]\boldsymbol{e}_{\boldsymbol{y}-\boldsymbol{x}}\,d\boldsymbol{y}. \tag{2.3.16}$$

The associated bilinear form is given by

$$a^\epsilon_{D,l}(\boldsymbol{u},\boldsymbol{v}) = \frac{g''(0)}{\epsilon^2}\int_D \omega(\boldsymbol{x})\theta(\boldsymbol{x};\boldsymbol{u})\theta(\boldsymbol{y};\boldsymbol{v})d\boldsymbol{x}. \tag{2.3.17}$$

The total force after linearization is

$$\mathcal{L}^\epsilon_l(\boldsymbol{u})(\boldsymbol{x}) = \mathcal{L}^\epsilon_{T,l}(\boldsymbol{u})(\boldsymbol{x}) + \mathcal{L}^\epsilon_{D,l}(\boldsymbol{u})(\boldsymbol{x}) \tag{2.3.18}$$

and the bilinear operator associated to $\mathcal{L}^\epsilon_l$ is given by

$$a^\epsilon_l(\boldsymbol{u},\boldsymbol{v}) = a^\epsilon_{T,l}(\boldsymbol{u},\boldsymbol{v}) + a^\epsilon_{D,l}(\boldsymbol{u},\boldsymbol{v}). \tag{2.3.19}$$

We have

$$(\mathcal{L}^\epsilon_l(\boldsymbol{u}),\boldsymbol{v}) = -a^\epsilon_l(\boldsymbol{u},\boldsymbol{v}).$$

We now discuss the stability of the FEM approximation to the linearized problem. Let $\boldsymbol{u}^k_{l,h}$ denote the approximate solution satisfying, for $k \geq 1$,

$$\left(\frac{\boldsymbol{u}^{k+1}_{l,h} - 2\boldsymbol{u}^k_{l,h} + \boldsymbol{u}^{k-1}_{l,h}}{\Delta t^2}, \tilde{\boldsymbol{u}}\right) = (\mathcal{L}^\epsilon_l(\boldsymbol{u}^k_{l,h}),\tilde{\boldsymbol{u}}) + (\boldsymbol{b}^k_h,\tilde{\boldsymbol{u}}), \qquad \forall \tilde{\boldsymbol{u}} \in V_h \tag{2.3.20}$$

and, for $k = 0$,

$$\left(\frac{\boldsymbol{u}^1_{l,h} - \boldsymbol{u}^0_{l,h}}{\Delta t^2}, \tilde{\boldsymbol{u}}\right) = \frac{1}{2}(\mathcal{L}^\epsilon(\boldsymbol{u}^0_{l,h}),\tilde{\boldsymbol{u}}) + \frac{1}{\Delta t}(\boldsymbol{v}^0_{l,h},\tilde{\boldsymbol{u}}) + \frac{1}{2}(\boldsymbol{b}^0_h,\tilde{\boldsymbol{u}}), \qquad \forall \tilde{\boldsymbol{u}} \in V_h. \tag{2.3.21}$$

The following notation will be used to define the discrete energy at each time step k

$$\begin{aligned}
&\overline{\boldsymbol{u}}^{k+1}_h := \frac{\boldsymbol{u}^{k+1}_h + \boldsymbol{u}^k_h}{2},\ \overline{\boldsymbol{u}}^k_h := \frac{\boldsymbol{u}^k_h + \boldsymbol{u}^{k-1}_h}{2},\\
&\bar{\partial}_t \boldsymbol{u}^k_h := \frac{\boldsymbol{u}^{k+1}_h - \boldsymbol{u}^{k-1}_h}{2\Delta t},\ \bar{\partial}^+_t \boldsymbol{u}^k_h := \frac{\boldsymbol{u}^{k+1}_h - \boldsymbol{u}^k_h}{\Delta t},\ \bar{\partial}^-_t \boldsymbol{u}^k_h := \frac{\boldsymbol{u}^k_h - \boldsymbol{u}^{k-1}_h}{\Delta t}.
\end{aligned} \tag{2.3.22}$$

We also define

$$\bar{\partial}_{tt}\boldsymbol{u}^k_h := \frac{\boldsymbol{u}^{k+1}_h - 2\boldsymbol{u}^k_h + \boldsymbol{u}^{k-1}_h}{\Delta t^2} = \frac{\bar{\partial}^+_t\boldsymbol{u}^k_h - \bar{\partial}^-_t\boldsymbol{u}^k_h}{\Delta t}.$$

We introduce the discrete energy associated with $\boldsymbol{u}^k_{l,h}$ at time step k as follows

$$\mathcal{E}(\boldsymbol{u}^k_{l,h}) := \frac{1}{2}\left[||\bar{\partial}^+_t\boldsymbol{u}^k_{l,h}||^2 - \frac{\Delta t^2}{4}a^\epsilon_l(\bar{\partial}^+_t\boldsymbol{u}^k_{l,h},\bar{\partial}^+_t\boldsymbol{u}^k_{l,h}) + a^\epsilon_l(\overline{\boldsymbol{u}}^{k+1}_{l,h},\overline{\boldsymbol{u}}^{k+1}_{l,h})\right]$$

Following [Theorem 4.1, [Karaa, 2012]], the stability of central difference scheme is given by

Theorem 2.3.2 ***Energy Stability of the Central difference approximation of linearized peridynamics***
Let $\boldsymbol{u}^k_{l,h}$ be the approximate solution of Equation 2.3.20 and Equation 2.3.21. In the absence of body force $\boldsymbol{b}(t) = 0$ for all t, if Δt satisfies the CFL like condition

$$\frac{\Delta t^2}{4} \sup_{\boldsymbol{u} \in V_h \setminus \{\boldsymbol{0}\}} \frac{a^\epsilon_l(\boldsymbol{u},\boldsymbol{u})}{(\boldsymbol{u},\boldsymbol{u})} \leq 1, \tag{2.3.23}$$

then the discrete energy is positive and we have the stability

$$\mathcal{E}(\boldsymbol{u}^k_{l,h}) = \mathcal{E}(\boldsymbol{u}^0_{l,h}). \tag{2.3.24}$$

2.4 Numerical experimants

In this section, we present numerical simulations that are consistent with the theoretical a-priori bound on the convergence rate. We also compare the peridynamic energy of the material softening zone and the classic Griffith's fracture energy of linear elastic fracture mechanics.

We consider Plexiglass at room temperature and specify the density $\rho = 1200\,kg/m^3$, bulk modulus $K = 25\,GPa$, Poisson's ratio $\nu = 0.245$, and critical energy release rate $G_c = 500\,Jm^{-2}$. The pairwise interaction and the hydrostatic interaction are characterized by potentials $f(r) = c(1 - \exp[-\beta r^2])$ and $g(r) = \bar{C}r^2/2$ respectively. Here we have used a quadratic hydrostatic interaction potential. The influence function is $J(r) = 1 - r$. Since pairwise potential f is symmetric for positive and negative strain the critical strain is given by $S_c(\boldsymbol{y}, bx) = \frac{\pm\bar{r}}{\sqrt{\boldsymbol{y}-\boldsymbol{x}}}$, where $\pm\bar{r}$ is the inflection point of $f(r)$ given by $\bar{r} = \frac{1}{\sqrt{\beta}}$. Following equations 94, 95, and 97 of [Lipton et al., 2018b], the relation between peridynamic material parameters and Lamé constants (λ, μ) and critical energy release rate G_c can be written as (for 2-d)

$$c = \frac{\pi G_c}{4M_J}, \qquad \beta = \frac{4\mu}{CM_J}, \qquad \bar{C} = \frac{2(\lambda - \mu)}{M_J^2}, \tag{2.4.1}$$

where M_J is given by

$$M_J = \int_0^1 J(r)r^2 dr = \frac{1}{12}.$$

By solving Equation 2.4.1, we get $c = 4712.4$, $\bar{C} = -1.7349 \times 10^{11}$, $\beta = 1.5647 \times 10^8$.

We consider a 2-d domain $D = [0, 0.1\,m]^2$ (with unit thickness in third direction) with vertical crack of length $0.02\,m$. The boundary conditions are described in Figure 3.2. The simulation time is $T = 40\,\mu s$ and the time step is $\Delta t = 0.004\,\mu s$. We consider two horizons $8\,mm$ and $4\,mm$. We run simulations for mesh sizes $h = 2, 1, 0.5\,mm$. We consider the central difference time discretization described by Equation 2.3.2 on a uniform mesh consisting of linear triangle elements. Second order quadrature approximation is used in the simulation for each triangle element. To reduce the load on memory and to avoid matrix-vector multiplication at each time step, we approximate the mass matrix by diagonal mass matrix using lumping (row-sum) technique. Suppose exact mass matrix is $\boldsymbol{M} = [m_{ij}]$ where m_{ij} is the element of $\boldsymbol{M}$ corresponding to i^{th} row and j^{th} column, then we approximate $\boldsymbol{M}$ by diagonal matrix $\hat{\boldsymbol{M}} = [\hat{m}_{ij}]$ where $\hat{m}_{ii} = \sum_j m_{ij}$ and $\hat{m}_{ij} = 0$ if $j \neq i$.

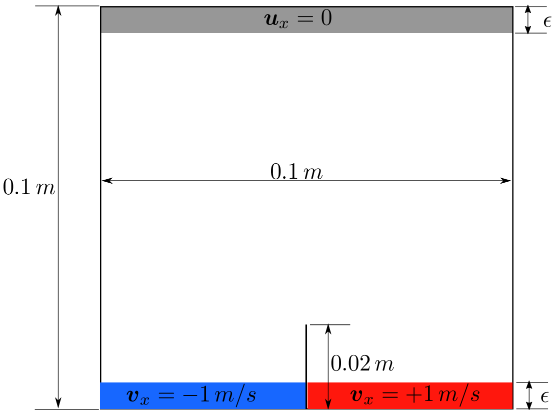

Figure 2.1: Material domain $D = [0, 0.1\,m]^2$ with crack of length $0.02\,m$. The x-component and y-component of displacement are fixed along a collar of thickness equal to the horizon on top. On the bottom the velocity $\boldsymbol{v}_x = \pm 1\,m/s$ along x-direction is specified on either side of the crack to make the crack propagate upwards.

2.4.1 Convergence rate

To compute convergence rate numerically we proceed as follows: consider a fixed horizon ϵ and three different mesh sizes h_1, h_2, h_3 such that $r = h_1/h_2 = h_2/h_3$. Let $\boldsymbol{u}_1, \boldsymbol{u}_2, \boldsymbol{u}_3$ be approximate solutions corresponding to meshes of size h_1, h_2, h_3, and let $\boldsymbol{u}$ be the exact solution. We write the error as $||\boldsymbol{u}_h - \boldsymbol{u}|| = Ch^\alpha$ for some constant C and $\alpha > 0$, to get

$$\log(||\boldsymbol{u}_1 - \boldsymbol{u}_2||) = C + \alpha \log h_2,$$
$$\log(||\boldsymbol{u}_2 - \boldsymbol{u}_3||) = C + \alpha \log h_3.$$

From above two equations, it is easy to see that the rate of convergence α is

$$\frac{\log(||\boldsymbol{u}_1 - \boldsymbol{u}_2||) - \log(||\boldsymbol{u}_2 - \boldsymbol{u}_3||)}{\log(r)}. \tag{2.4.2}$$

The convergence result for horizons $\epsilon = 8\,mm$ and $\epsilon = 4\,mm$ is shown in Figure 3.5. In the simulation we have considered second order approximation of integration using quadrature points. The simulations show a rate of convergence that agrees with the a-priori estimates given in Theorem 3.3.3.

2.4.2 Fracture energy of crack zone

The extent of damage at material point $\boldsymbol{x}$ is given by the function $Z(\boldsymbol{x})$

$$Z(\boldsymbol{x}) = \max_{\boldsymbol{y} \in H_\epsilon(\boldsymbol{x}) \cap D} \frac{S(\boldsymbol{y}, \boldsymbol{x}; \boldsymbol{u})}{S_c^+}. \tag{2.4.3}$$

The crack zone is defined as set of material points which have $Z > 1$. We compute the peridynamic energy of crack zone and compare it with the Griffith's fracture energy. For a crack of length l, the Griffith's fracture energy (G.E.) will be $G.E. = G_c \times l$. The

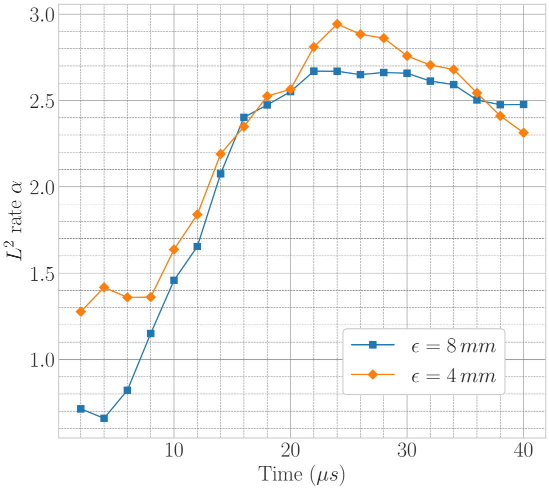

Figure 2.2: Convergence rate at different times for two horizons. For both horizons $\epsilon = 4, 8\,mm$, the three meshes of size $h = 2, 1, 0.5\,mm$ were considered to compute the convergence rate.

peridynamic fracture energy (P.E.) associated with the material softening zone is given by

$$P.E. = \int_{\substack{\boldsymbol{x}\in D,\\ Z(\boldsymbol{x})\geq 1}} \left[\frac{1}{\epsilon^d \omega_d}\int_{H_\epsilon(\boldsymbol{x})} |\boldsymbol{y}-\boldsymbol{x}|\mathcal{W}^\epsilon(S(\boldsymbol{y},\boldsymbol{x};\boldsymbol{u}))\,d\boldsymbol{y}\right] d\boldsymbol{x} + \int_{\substack{\boldsymbol{x}\in D,\\ Z(\boldsymbol{x})\geq 1}} \mathcal{V}^\epsilon(\theta(\boldsymbol{x},t;\boldsymbol{u}))\,d\boldsymbol{x}$$

where $\mathcal{W}^\epsilon(S(\boldsymbol{y},\boldsymbol{x};\boldsymbol{u}))$ is the bond-based potential, see Equation 1.2.2 and $\mathcal{V}^\epsilon(\theta(\boldsymbol{x},t;\boldsymbol{u}))$ is the hydrostatic interaction potential, see Equation 1.2.4.

In Figure 2.3 classical fracture energy and peridynamic fracture energy is shown at different crack length. The error in both energies at different times is shown in Figure 2.4. The agreement between two energies is good. The damage profile at time $30\,\mu s$ and $40\,\mu s$ is shown in Figure 2.5. At each node, the damage function Z is computed by treating edges between mesh nodes as bonds. In addition to the damage plots, we show velocity profile at $30\,\mu s$ and $40\,\mu s$ in Figure 2.6. In Figure 2.7 we show the plot of the xx component of symmetric gradient of the displacement. Here the region for which the magnitude of the strain is greater than a multiple of the critical strain is the yellow region. It is seen that the high strain region surrounds the crack.

As the crack is propagating vertically it is seen that the high strain region is next to the crack i

2.5 Concluding remarks on the FEM method for nonlocal fracture modeling

We have provided a-priori error estimates for finite element approximations to nonlocal state based peridynamic fracture models. We have shown that the convergence rate applies

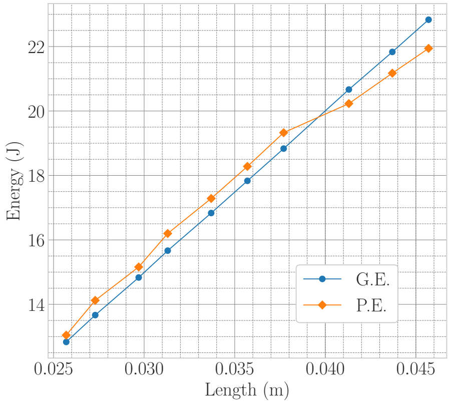

Figure 2.3: Peridynamic energy and Griffith's energy as a function of crack length.

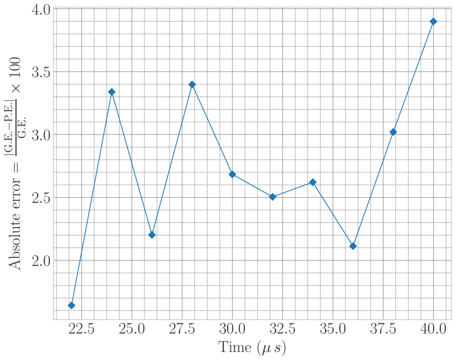

Figure 2.4: Error between Peridynamic energy and Griffith's energy at different times.

even over time intervals for which the material is softening over parts of the computational domain. The results are established for two different classes of state-based peridynamic forces. The convergence rate of the approximation is of the form $C(\Delta t + h^2/\epsilon^2)$ where the constant C depends on ϵ and the H^2 norm of the solution and its time derivatives. For fixed Δt numerical simulations for Plexiglass show that the error decreases at the rate of h^2 at 40μ-sec into the simulation. The simulations were carried out in parallel using 20 threads on an workstation with single Intel Xeon processor and with 32 GB of RAM. We anticipate similar convergence rates for longer times on bigger parallel machines. We note that we will also have convergence rates if the spatial regularity of the evolution is in the Sobelev spaces H^1. However for this case we can show the convergence rate is the same as for the finite difference method discussed in the next section. Because the finite difference method is simpler to implement and offers less computational complexity than FEM we do not discuss the H^1 FEM and instead discuss the finite difference method in the following section.

In conclusion we reiterate that the a-priori error estimates account for the possible appearance of nonlinearity anywhere in the computational domain. On the other hand numerical simulation and independent theoretical estimates show that the nonlinearity concentrates along "fat" cracks of finite length and width equal to ϵ, see [Lipton, 2016, Lipton, 2014]. Moreover the remainder of the computational domain is seen to behave

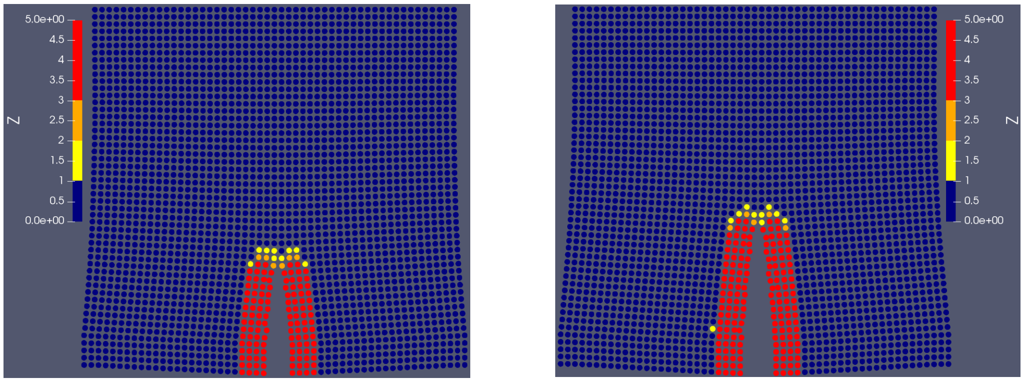

(a) $t = 30\,\mu s$ (b) $t = 40\,\mu s$

Figure 2.5: Color plot of damage function Z on deformed material domain at time $t = 30\,\mu s$ and $40\,\mu s$. Dark blue represents undamaged material $Z < 1$, $Z \approx 1$ is yellow at crack tip, red is softening material. Here, the displacements are scaled by 100 and damage function is cut off at 5 to highlight the crack zone.

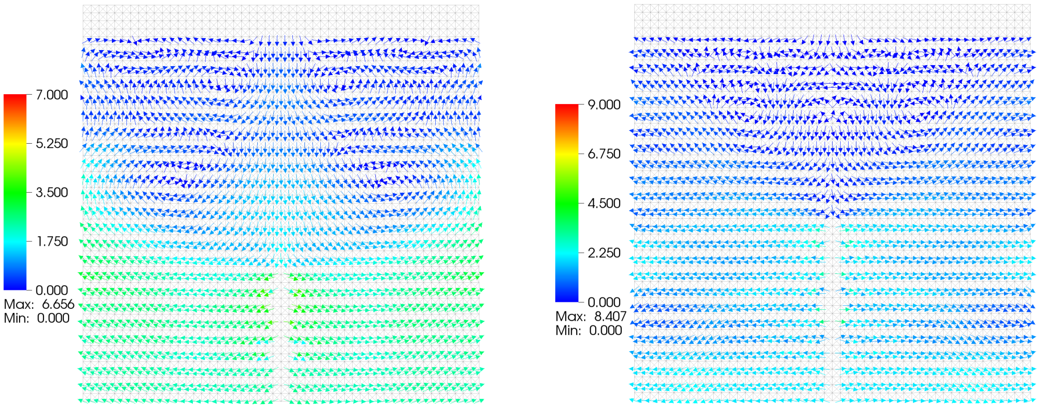

(a) $t = 30\,\mu s$ (b) $t = 40\,\mu s$

Figure 2.6: Velocity profile.

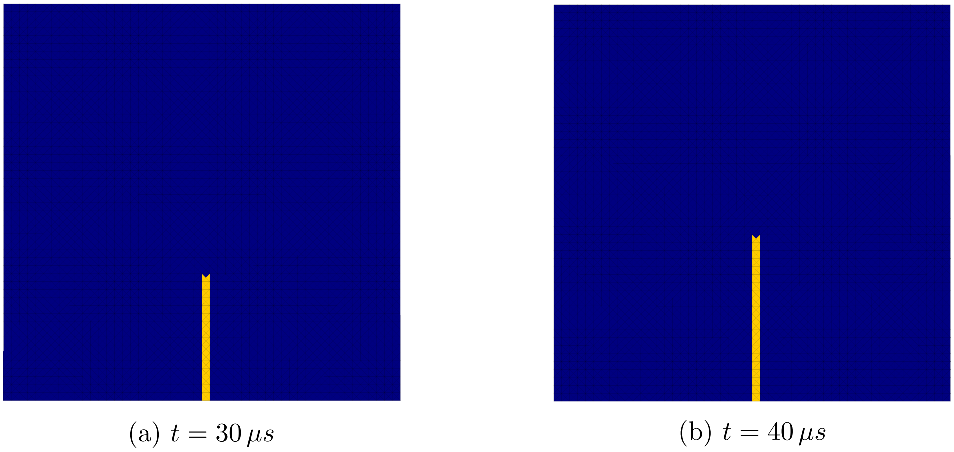
(a) $t = 30\,\mu s$ (b) $t = 40\,\mu s$

Figure 2.7: Magnitude of the xx component of strain $\nabla \boldsymbol{u} + \nabla \boldsymbol{u}^T$. The region for which the magnitude of the strain is greater than a multiple of the critical strain is the yellow region

linearly and to leading order can be modeled as a linear elastic material up to an error proportional to ϵ, see [Proposition 6, [Jha and Lipton 2018b]]. Future work will use these observations to focus on adaptive implementation and a-posteriori estimates.

Chapter 3

Finite difference approximation to nonlocal fracture models

3.1 Introduction

In this project published in [Jha and Lipton, 2018a] the new contributions are a-priori convergence rates for finite difference methods applied to state based peridynamic models. As mentioned earlier the constitutive behavior is non-linear, non-convex and material properties can degrade during the course of the evolution. Here we consider the class of Hölder continuous displacement fields and show the existence of a unique Hölder continuous evolution for a prescribed Hölder continuous initial condition and body force, see Theorem 3.2.2. To obtain a-priori bounds on the error, we construct the L^2 approximation theory for the finite difference approximation in the spatial variables and the forward Euler approximation in time, see section 3.3. Hölder continuous solutions are not differentiable and strains are written as difference quotients. As before the fracture set is approximated by regions with softening forces with large strains. The model naturally localizes the fracture set in the computational simulations. We show that discrete approximations converge to the exact Hölder continuous solution uniformly over finite time intervals with respect to the L^2 norm. The a-priori rate of convergence in the L^2 norm is given by $(C_t \Delta t + C_s h^\gamma / \epsilon^2)$, where Δt is the size of the time step, h is the size of spatial mesh discretization, $\gamma \in (0, 1]$ is the Hölder exponent, and ϵ is the length scale of nonlocal interaction relative to the size of the domain, see Theorem 3.3.3 The constant C_t depends on the L^2 norm of the time derivatives of the solution, C_s depends on the Hölder norm of the solution and the Lipschitz constant of peridynamic force. We point out that the convergence results derived here can be extended to general single step time discretization using arguments provided in [Jha and Lipton, 2018a]. Although the constitutive law relating force to strain is nonlinear we are still able to establish stability for the semi-discrete approximation and it is shown that the energy at any given time t is bounded above by the energy of the initial conditions and the total work done by the body force up to time t, see Theorem 3.3.2. We provide the connection between the non-dimensionalized dynamics used in the a-priori convergence analysis and the simulated dynamics using dimensional quantities, see section 3.4. The numerics are carried out for plexiglass. Our numerical simulations are consistent with the theoretical studies, see section 3.5. In the simulations we introduce a straight crack and it propagates in response to applied boundary conditions. For these simulations we use piecewise constant interpolants and record the rate of convergence with respect to mesh size while keeping the horizon fixed. Our results show that convergence rate remains above the a-priori estimated rate during the simulation. For illustration we also present numerical simulations for a pre-cracked samples subject to a bending load.

3.2 Existence of solutions

Let $C^{0,\gamma}(D;\mathbb{R}^d)$ be the Hölder space with exponent $\gamma \in (0,1]$. We introduce $C_0^{0,\gamma}(D) = C^{0,\gamma}(D) \cap C_0(D)$ where $C_0(D)$ is the closure of continuous functions with compact support on D in the supremum norm. Functions in $C_0(D)$ are uniquely extended to $\overline{D}$ and take zero values on ∂D. We extend all functions in $C_0^{0,\gamma}(D)$ by zero outside D. The norm of $\boldsymbol{u} \in C_0^{0,\gamma}(D;\mathbb{R}^d)$ is given by

$$\|\boldsymbol{u}\|_{C^{0,\gamma}(D;\mathbb{R}^d)} := \sup_{\boldsymbol{x}\in D} |\boldsymbol{u}(\boldsymbol{x})| + [\boldsymbol{u}]_{C^{0,\gamma}(D;\mathbb{R}^d)},$$

where $[\boldsymbol{u}]_{C^{0,\gamma}(D;\mathbb{R}^d)}$ is the Hölder semi norm and given by

$$[\boldsymbol{u}]_{C^{0,\gamma}(D;\mathbb{R}^d)} := \sup_{\substack{\boldsymbol{x}\neq\boldsymbol{y},\\ \boldsymbol{x},\boldsymbol{y}\in D}} \frac{|\boldsymbol{u}(\boldsymbol{x}) - \boldsymbol{u}(\boldsymbol{y})|}{|\boldsymbol{x}-\boldsymbol{y}|^\gamma},$$

and $C_0^{0,\gamma}(D;\mathbb{R}^d)$ is a Banach space with this norm. Here we make the hypothesis that the domain function ω belongs to $C_0^{0,\gamma}(D;[0,1])$.

We consider the first order system of equations equivalent to Equation 1.2.11. Let $y_1(t) = \boldsymbol{u}(t)$, $y_2(t) = \boldsymbol{v}(t)$ with $\boldsymbol{v}(t) = \dot{\boldsymbol{u}}(t)$. We form the vector $y = (y_1, y_2)^T$ where $y_1, y_2 \in C_0^{0,\gamma}(D;\mathbb{R}^d)$ and let $F^\epsilon(y,t) = (F_1^\epsilon(y,t), F_2^\epsilon(y,t))^T$ with

$$F_1^\epsilon(y,t) := y_2 \tag{3.2.1}$$

$$F_2^\epsilon(y,t) := \mathcal{L}^\epsilon(y_1(t)) + \boldsymbol{b}(t). \tag{3.2.2}$$

We point out here that the domain function ω insures that $F^\epsilon(y,t)$ maps into $C_0^{0,\gamma}(D;\mathbb{R}^d) \times C_0^{0,\gamma}(D;\mathbb{R}^d)$. The initial boundary value associated with the evolution Equation 1.2.11 is equivalent to the initial boundary value problem for the first order system given by

$$\frac{d}{dt} y = F^\epsilon(y,t), \tag{3.2.3}$$

with initial condition given by $y(0) = (\boldsymbol{u}_0, \boldsymbol{v}_0)^T \in C_0^{0,\gamma}(D;\mathbb{R}^d) \times C_0^{0,\gamma}(D;\mathbb{R}^d)$.

We next show that $F^\epsilon(y,t)$ is Lipschitz continuous.

Proposition 3.2.1 ***Lipschitz continuity and bound***
Let $X = C_0^{0,\gamma}(D;\mathbb{R}^d) \times C_0^{0,\gamma}(D;\mathbb{R}^d)$. We suppose that the boundary function ω belongs to $C_0^{0,\gamma}(D;[0,1])$. Let f be a convex-concave function satisfying $C_i^f < \infty$ for $i = 0,..,4$ and let g either be a quadratic function, or g be a convex-concave function with $C_i^g < \infty$ for $i = 0,..,4$, then the function $F^\epsilon(y,t) = (F_1^\epsilon, F_2^\epsilon)^T$, as defined in Equation 3.2.1 and

Equation 3.2.2, is Lipschitz continuous in any bounded subset of X. *We have, for any* $y, z \in X$ *and* $t > 0$,

$$\begin{aligned} &\|F^\epsilon(y,t) - F^\epsilon(z,t)\|_X \\ &\leq \frac{L_1(1 + ||\omega||_{C^{0,\gamma}})(1 + ||y||_X + ||z||_X)}{\epsilon^{2+\alpha(\gamma)}}||y - z||_X. \end{aligned} \tag{3.2.4}$$

where L_1 *is independent of* $\boldsymbol{u}, \boldsymbol{v}$ *and* ϵ, *and depends on* f, J, *and* g. *The exponent* $\alpha(\gamma)$ *is* 0 *if* $\gamma \geq 1/2$ *and is* $1/2 - \gamma$ *if* $\gamma \leq 1/2$. *Furthermore, for any* $y \in X$ *and any* $t \in [0, T]$, *we have the bound*

$$\|F^\epsilon(y,t)\|_X \leq \frac{L_2(1 + ||\omega||_{C^{0,\gamma}})(1 + ||y||_X)}{\epsilon^2} + b, \tag{3.2.5}$$

where $b = \sup_t \|\boldsymbol{b}(t)\|_{C^{0,\gamma}(D;\mathbb{R}^d)}$ *and* L_2 *is independent of* y.

We easily see that on choosing $z = 0$ in Equation 3.2.4 that $\mathcal{L}^\epsilon(\boldsymbol{u})$ is in $C^{0,\gamma}(D;\mathbb{R}^d)$ provided that $\boldsymbol{u}$ belongs to $C^{0,\gamma}(D;\mathbb{R}^3)$. Moreover since $\mathcal{L}^\epsilon(\boldsymbol{u})$ takes the value $\mathbf{0}$ on ∂D we can conclude that $\mathcal{L}^\epsilon(\boldsymbol{u})$ also belongs to $C_0^{0,\gamma}(D;\mathbb{R}^d)$.

The following theorem gives the existence and uniqueness of solution in any given time domain $I_0 = (-T, T)$.

Theorem 3.2.2 ***Existence and uniqueness of Hölder solutions over finite time intervals***
Let f *be a convex-concave function satisfying* $C_i^f < \infty$ *for* $i = 0, .., 4$ *and let* g *either be a quadratic function, or* g *be a convex-concave function with* $C_i^g < \infty$ *for* $i = 0, .., 4$. *For any initial condition* $x_0 \in X = C_0^{0,\gamma}(D;\mathbb{R}^d) \times C_0^{0,\gamma}(D;\mathbb{R}^d)$, *time interval* $I_0 = (-T, T)$, *and right hand side* $\boldsymbol{b}(t)$ *continuous in time for* $t \in I_0$ *such that* $\boldsymbol{b}(t)$ *satisfies* $\sup_{t \in I_0} ||\boldsymbol{b}(t)||_{C^{0,\gamma}} < \infty$, *there is a unique solution* $y(t) \in C^1(I_0; X)$ *of*

$$y(t) = x_0 + \int_0^t F^\epsilon(y(\tau), \tau)\, d\tau, \tag{3.2.6}$$

or equivalently

$$y'(t) = F^\epsilon(y(t), t), \text{with } y(0) = x_0, \tag{3.2.7}$$

where $y(t)$ *and* $y'(t)$ *are Lipschitz continuous in time for* $t \in I_0$.

We conclude this section by stating the following result which shows the Lipschitz bound of peridynamic force in L^2 norm for functions in $L_0^2(D;\mathbb{R}^d)$. Here $L_0^2(D;\mathbb{R}^d)$ denotes the space of functions $\boldsymbol{u} \in L^2(D;\mathbb{R}^d)$ such that $\boldsymbol{u} = \mathbf{0}$ on ∂D. We assume that functions in $L_0^2(D;\mathbb{R}^d)$ are extended to $\mathbb{R}^d$ by zero.

Proposition 3.2.3 ***Lipschitz continuity of peridynamic force in*** L^2
Let f *and* g *satisfy the hypothesis of Theorem 3.2.2, then for any* $\boldsymbol{u}, \boldsymbol{v} \in L_0^2(D;\mathbb{R}^d)$ *we have*

$$||\mathcal{L}^\epsilon(\boldsymbol{u}) - \mathcal{L}^\epsilon(\boldsymbol{v})||_{L^2(D;\mathbb{R}^d)} \leq \frac{L_3}{\epsilon^2}||\boldsymbol{u} - \boldsymbol{v}||_{L^2(D;\mathbb{R}^d)}, \tag{3.2.8}$$

where the constants L_3 *and* L_4 *are independent of* ϵ, $\boldsymbol{u}$ *and* $\boldsymbol{v}$. *Here* $L_3 = 4(C_1^f \bar{J}_1 + C_2^g \bar{J}_0^2)$, *for convex-concave* g, *and* $L_3 = 4(C_1^f \bar{J}_1 + g''(0)\bar{J}_0^2)$, *for quadratic* g. *Here* $\bar{J}_\alpha = \frac{1}{\omega_d}\int_{H_1(\mathbf{0})} J(|\boldsymbol{\xi}|)|\boldsymbol{\xi}|^{-\alpha} d\boldsymbol{\xi}$.

We now describe the finite difference scheme and give the rate of convergence to Hölder continuous solutions of the nonlocal equation of motion.

3.3 Finite difference approximation

In this section we consider the discrete approximation to the dynamics given by finite differences in space and the forward Euler discretization in time. Let h denote the mesh size and $D_h = D \cap (h\mathbb{Z})^d$ be the associated discretization of the material domain D. In this paper we will keep the horizon length scale ϵ fixed and assume that the spatial discretization length satisfies $h < \epsilon < 1$. Let $i \in \mathbb{Z}^d$ be the index such that $\boldsymbol{x}_i = hi \in D$, see Figure 3.1. Let U_i be a the cell of volume h^d corresponding to the grid point $\boldsymbol{x}_i$. The exact solution evaluated at grid points is denoted by $(\boldsymbol{u}_i(t), \boldsymbol{v}_i(t))$. Given any discrete set $\{\hat{\boldsymbol{u}}_i\}_{i,\boldsymbol{x}_i \in D}$, where i is index representing grid point of mesh, we define its piecewise constant extension as

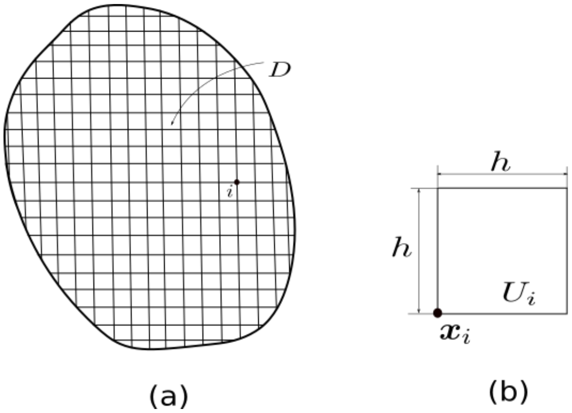

Figure 3.1: (a) Typical mesh of size h. (b) Unit cell U_i corresponding to material point $\boldsymbol{x}_i$.

$$\hat{\boldsymbol{u}}(\boldsymbol{x}) := \sum_{i,\boldsymbol{x}_i \in D} \hat{\boldsymbol{u}}_i \chi_{U_i}(\boldsymbol{x}). \tag{3.3.1}$$

In this way we have representation of the discrete set as a piecewise constant function.

We now describe the L^2-projection of the function $\boldsymbol{u} : D \to \mathbb{R}^d$ onto the space of piecewise constant functions defined over the cells U_i. We denote the average of $\boldsymbol{u}$ over the unit cell U_i as $\tilde{\boldsymbol{u}}_i$ and

$$\tilde{\boldsymbol{u}}_i := \frac{1}{h^d} \int_{U_i} \boldsymbol{u}(\boldsymbol{x}) d\boldsymbol{x} \tag{3.3.2}$$

and the L^2 projection of $\boldsymbol{u}$ onto piecewise constant functions is $\tilde{\boldsymbol{u}}$ given by

$$\tilde{\boldsymbol{u}}(\boldsymbol{x}) := \sum_{i,\boldsymbol{x}_i \in D} \tilde{\boldsymbol{u}}_i \chi_{U_i}(\boldsymbol{x}). \tag{3.3.3}$$

Lemma 3.3.1 *Let $\boldsymbol{u} \in C_0^{0,\gamma}(D;\mathbb{R}^d)$ and let $\tilde{\boldsymbol{u}}$ be its L^2 projection defined in Equation 3.3.3, then we have*

$$|\tilde{\boldsymbol{u}}(\boldsymbol{x}) - \boldsymbol{u}(\boldsymbol{x})| \leq [c^\gamma ||\boldsymbol{u}||_{C^{0,\gamma}}]\, h^\gamma, \forall \boldsymbol{x} \in D,$$
$$||\tilde{\boldsymbol{u}}(\boldsymbol{x}) - \boldsymbol{u}(\boldsymbol{x})||_{L^2} \leq \left[c^\gamma \sqrt{|D|} ||\boldsymbol{u}||_{C^{0,\gamma}}\right] h^\gamma, \tag{3.3.4}$$

where $c = \sqrt{2}$ for $d = 2$ and $c = \sqrt{3}$ for $d = 3$.

This lemma can be demonstrated easily by substituting Equation 3.3.3 for $\tilde{\boldsymbol{u}}$ and using the fact that $\boldsymbol{u} \in C_0^{0,\gamma}(D;\mathbb{R}^d)$. We also note that first line of Equation 3.3.4 remains valid of $\boldsymbol{x}$ in a layer of thickness 2ϵ surrounding D.

3.3.1 Stability of the semi-discrete approximation

We first introduce the semi-discrete boundary condition by setting $\hat{\boldsymbol{u}}_i(t) = \boldsymbol{0}$ for all t and for all $\boldsymbol{x}_i \notin D$. Let $\{\hat{\boldsymbol{u}}_i(t)\}_{i,\boldsymbol{x}_i \in D}$ denote the semi-discrete approximate solution which satisfies the following, for all $t \in [0,T]$ and i such that $\boldsymbol{x}_i \in D$,

$$\ddot{\hat{\boldsymbol{u}}}_i(t) = \mathcal{L}^\epsilon(\hat{\boldsymbol{u}}(t))(\boldsymbol{x}_i) + \boldsymbol{b}(\boldsymbol{x}_i, t), \tag{3.3.5}$$

where $\hat{\boldsymbol{u}}(t)$ is the piecewise constant extension of discrete set $\{\hat{\boldsymbol{u}}_i(t)\}_i$ and is defined as

$$\hat{\boldsymbol{u}}(\boldsymbol{x}, t) = \begin{cases} \sum_{i,\boldsymbol{x}_i \in D} \hat{\boldsymbol{u}}_i(t) \chi_{U_i}(\boldsymbol{x}), \\ \boldsymbol{0}, \;\; i, \text{ such that } \boldsymbol{x}_i \notin D. \end{cases} \tag{3.3.6}$$

The scheme is complemented with the discretized initial conditions $\hat{\boldsymbol{u}}_i(0) = \boldsymbol{u}_0(\boldsymbol{x}_i)$ and $\hat{\boldsymbol{v}}_i(0) = \boldsymbol{v}_0(\boldsymbol{x}_i)$.

The total kinetic and potential energy is given by

$$\mathcal{E}^\epsilon(\boldsymbol{u})(t) = \frac{1}{2}||\dot{\boldsymbol{u}}(t)||^2_{L^2} + PD^\epsilon(\boldsymbol{u}(t)),$$

and we introduce the augmented energy given by

$$\bar{\mathcal{E}}^\epsilon(\boldsymbol{u})(t) := \mathcal{E}^\epsilon(\boldsymbol{u})(t) + \frac{1}{2}||\boldsymbol{u}(t)||^2_{L^2}. \tag{3.3.7}$$

We have the stability of the semi-discrete evolution.

Theorem 3.3.2 ***Energy stability of the semi-discrete approximation***
Let $\{\hat{\boldsymbol{u}}_i(t)\}_{i,\boldsymbol{x}_i \in D}$ be the solution to the semidiscrete initial boundary value problem Equation 3.3.5 and $\hat{\boldsymbol{u}}(t)$ denote its piecewise constant extension. Similarly let $\hat{\boldsymbol{b}}(t,\boldsymbol{x})$ denote the piecewise constant extension of $\{\boldsymbol{b}(t,\boldsymbol{x}_i)\}_{i,\boldsymbol{x}_i \in D}$. If f and g are convex-concave type functions satisfying the hypotheses of Theorem 3.2.2, then the total energy $\mathcal{E}^\epsilon(\hat{\boldsymbol{u}})(t)$ satisfies,

$$\mathcal{E}^\epsilon(\hat{\boldsymbol{u}})(t) \leq \left(\sqrt{\mathcal{E}^\epsilon(\hat{\boldsymbol{u}})(0)} + \frac{tC}{\epsilon^2} + \int_0^t ||\hat{\boldsymbol{b}}(s)||_{L^2} ds\right)^2, \;\forall t \in [0,T], \tag{3.3.8}$$

and the constant C is independent of ϵ and h.

If f is a convex-concave type function as above and g is quadratic then the augmented energy $\bar{\mathcal{E}}^\epsilon(\hat{\boldsymbol{u}})(t)$ satisfies,

$$\bar{\mathcal{E}}^\epsilon(\hat{\boldsymbol{u}})(t) \leq \exp[3(C_2/\epsilon^2+1)t]\Bigg(\bar{\mathcal{E}}^\epsilon(\hat{\boldsymbol{u}})(0) + \int_0^T (\frac{C_1^2}{\epsilon^4} + ||\hat{\boldsymbol{b}}(s)||^2_{L^2}) \exp[-3(C_2/\epsilon^2+1)s]ds\Bigg), \ \forall t \in [0,T], \tag{3.3.9}$$

where the constants C_1 and C_2 are independent of ϵ and h.

3.3.2 Time discretization

Let Δt be the size of the time step and $[0,T] \cap (\Delta t\mathbb{Z})$ be the discretization of the time domain. We denote the fully discrete solution at $(t^k = k\Delta t, \boldsymbol{x}_i = ih)$ as $(\hat{\boldsymbol{u}}_i^k, \hat{\boldsymbol{v}}_i^k)$ and the exact solution as $(\boldsymbol{u}_i^k, \boldsymbol{v}_i^k)$. We enforce the boundary condition $\hat{\boldsymbol{u}}_i^k = \boldsymbol{0}$ for all $\boldsymbol{x}_i \notin D$ and for all k. The piecewise constant extension of $\{\hat{\boldsymbol{u}}_i^k\}_{i\in\mathbb{Z}^d}$ and $\{\hat{\boldsymbol{v}}_i^k\}_{i\in\mathbb{Z}^d}$ are denoted by $\hat{\boldsymbol{u}}^k$ and $\hat{\boldsymbol{v}}^k$ respectively. The L^2-projection of $\boldsymbol{u}^k$ and $\boldsymbol{v}^k$ onto piecewise constant functions are denoted by $\tilde{\boldsymbol{u}}^k$ and $\tilde{\boldsymbol{v}}^k$ respectively.

The forward Euler time discretization, with respect to velocity, and the finite difference scheme for $(\hat{\boldsymbol{u}}_i^k, \hat{\boldsymbol{v}}_i^k)$ is written

$$\frac{\hat{\boldsymbol{u}}_i^{k+1} - \hat{\boldsymbol{u}}_i^k}{\Delta t} = \hat{\boldsymbol{v}}_i^{k+1} \tag{3.3.10}$$

$$\frac{\hat{\boldsymbol{v}}_i^{k+1} - \hat{\boldsymbol{v}}_i^k}{\Delta t} = \mathcal{L}^\epsilon(\hat{\boldsymbol{u}}^k)(\boldsymbol{x}_i) + \boldsymbol{b}_i^k. \tag{3.3.11}$$

The initial condition is enforced by setting $\hat{\boldsymbol{u}}_i^0 = (\hat{\boldsymbol{u}}_0)_i$ and $\hat{\boldsymbol{v}}_i^0 = (\hat{\boldsymbol{v}}_0)_i$. We note that the forward difference scheme for the system reduces to the central difference scheme for the second order differential equation Equation 1.2.11 on substitution of Equation 3.3.10 into Equation 3.3.11.

Convergence of approximation

In this section we provide an upper bound on the convergence rate of the fully discrete approximation to the Hölder continuous solution as measured by the L^2 norm. The L^2 approximation error E^k at time t^k, for $0 < t^k \leq T$, given by

$$E^k := \left\|\hat{\boldsymbol{u}}^k - \boldsymbol{u}^k\right\|_{L^2(D;\mathbb{R}^d)} + \left\|\hat{\boldsymbol{v}}^k - \boldsymbol{v}^k\right\|_{L^2(D;\mathbb{R}^d)}.$$

The following theorem gives an explicit a-priori upper bound on the convergence rate.

Theorem 3.3.3 ***Convergence of finite difference approximation (forward Euler time discretization)***
Let $\epsilon > 0$ be fixed. Let $(\boldsymbol{u}, \boldsymbol{v})$ be the solution of peridynamic equation Equation 3.2.3. We assume $\boldsymbol{u}, \boldsymbol{v} \in C^2([0,T]; C_0^{0,\gamma}(D;\mathbb{R}^d))$. Then the finite difference scheme given by Equation 3.3.10 and Equation 3.3.11 is consistent in both time and spatial discretization and converges to the exact solution uniformly in time with respect to the $L^2(D;\mathbb{R}^d)$ norm. If

we assume the error at the initial step is zero then the error E^k at time t^k is bounded and satisfies

$$\sup_{0\le k\le T/\Delta t} E^k \le O\left(C_t\Delta t + C_s\frac{h^\gamma}{\epsilon^2}\right), \tag{3.3.12}$$

where constant C_s and C_t are independent of h and Δt and C_s depends on the Hölder norm of the solution and C_t depends on the L^2 norms of time derivatives of the solution.

Here we have assumed the initial error is zero for ease of exposition only.

We remark that the explicit constants leading to Equation 3.3.12 can be large. The inequality that delivers Equation 3.3.12 is given by

$$\sup_{0\le k\le T/\Delta t} E^k \le \exp\left[T(1+L_3/\epsilon^2)\right] T\left[C_t\Delta t + (C_s/\epsilon^2)h^\gamma\right]. \tag{3.3.13}$$

The explicit constant C_t depends on the spatial L^2 norm of the time derivatives of the solution and C_s depends on the spatial Hölder continuity of the solution and the constant L_3. The constant L_3 is bounded independently of horizon ϵ. Although the constants are necessarily pessimistic they deliver a-priori error estimates. We provide the connection between the non-dimensionalized dynamics used in the a-priori convergence analysis and the simulated dynamics using dimensional quantities in section 3.4. We carry out numerical simulations for different values of the horizon ϵ in section 3.5. We find that the convergence rate for piecewise constant finite difference interpolation functions is greater than or equal to $\gamma = 1$ for simulations lasting in the tens of microseconds. These results are seen to be consistent with the a-priori estimates given in Theorem 3.3.3 above.

3.4 Quantifying the error

In this section we show how to apply the a-priori error bound to numerical simulations carried out using quantities with dimensions. As an example we consider the numerical simulation of a propagating crack in plexiglass at room temperature. Here the dynamics is modeled in terms of quantities with dimensions. We show how to transform the peridynamic equation of motion for Plexiglass into an equivalent evolution in terms of non dimensional quantities Equation 1.2.11. We then apply our a-priori error bounds to the equivalent non dimensional peridynamics subsection 3.3.2. In this way obtain the dimensionless simulation time for which the error remains within an acceptable limit. One can then transform the dimensionless time back to the actual time of the fracture propagation given in microseconds for which the a-priori simulation error is acceptable. We find that the acceptable simulation time predicted by a-priori analysis is smaller than can be seen in the numerical experiments. This is to be expected as a-priori estimates are naturally pessimistic. We explain the reasons for this difference in the last part of this section. To keep the following presentation simple, we will assume that the dimension is 2, the potential function $g = 0$ and $\boldsymbol{b} = \boldsymbol{0}$.

Suppose $\bar{D}$ is the material domain with characteristic length scale L_0 and suppose $\bar{\boldsymbol{x}} \in \bar{D}$ are coordinates with dimensions of length. Let $\bar{T}$ denote the simulation time with dimensions of time and $\bar{t} \in [0, \bar{T}]$. Let $\bar{\epsilon}$ denote the size of horizon with units of length. The displacement field is $\bar{\boldsymbol u}(\bar{\boldsymbol x},\bar t)$ and has units of length. The influence function $\bar J(\bar\xi) = a(1-\xi)$ is non dimensional and its argument $\bar\xi = |\bar{\boldsymbol x}-\bar{\boldsymbol y}|/\bar\epsilon$ is also non dimensional. The non dimensional parameter $a > 0$ is a fixed positive constant. Last we note that the boundary function ω is dimensionless and its argument is also dimensionless.

To fix ideas we consider an explicit potential function $\bar f(\bar r) = \bar C(1-\exp[-\bar\beta\bar r^2])$ where $\bar r$ has units of $\sqrt{\text{length}}$, $\bar C$ has units of force/length, and $\bar\beta$ has units of 1/length. Let the bulk modulus K, density $\bar\rho$, and critical energy release rate G correspond to Plexiglass at room temperature. Following equations 94, 95, and 97 of [Lipton et al., 2018b], the parameters $\bar C, \bar\beta$ are given by

$$\bar C = \frac{G}{2(\omega_1/\omega_2)M}, \quad \bar\beta = \frac{\lambda}{(1/4)\bar C M}, \quad M = \int_0^1 \bar J(\xi)\xi^2 d\xi, \tag{3.4.1}$$

where $\omega_1 = 2, \omega_2 = \pi$. Here the Lamé parameter is related to K by $\lambda = 3K/5$. For $\bar J(\xi) = a(1-\xi)$, $M = a/12$. Substituting, we have

$$\bar C = \frac{3\pi G}{a}, \quad \bar\beta = \frac{48K}{5\pi G} \tag{3.4.2}$$

and also

$$\bar C\bar\beta = \frac{144}{5a}K. \tag{3.4.3}$$

The solution $\bar{\boldsymbol u}$ satisfies

$$\bar\rho\ddot{\bar{\boldsymbol u}}(\bar{\boldsymbol x},\bar t) = \bar{\mathcal L}^{\bar\epsilon}_T(\bar{\boldsymbol u})(\bar{\boldsymbol x},\bar t), \qquad \forall(\bar{\boldsymbol x},\bar t) \in \bar D\times[0,\bar T]. \tag{3.4.4}$$

The solution $\bar{\boldsymbol u}$ takes the boundary condition $\bar{\boldsymbol u}(t) = \mathbf{0}$ for all $\bar{\boldsymbol x} \in \partial\bar D$ and the initial condition $\bar{\boldsymbol u}(0) = \bar{\boldsymbol u}_0, \dot{\bar{\boldsymbol u}}(0) = \bar{\boldsymbol v}_0$.

3.4.1 Nondimensionalization

Now we associate a local wave speed for the peridynamic material and an associated local time scale given by

$$v_0 = \sqrt{\frac{\bar C\bar\beta}{\bar\rho}}, \quad T_0 = \frac{L_0}{v_0}. \tag{3.4.5}$$

The change to non-dimensional variables is given by

$$x = \frac{\bar{\boldsymbol x}}{L_0}, \quad t = \frac{\bar t}{T_0}, \quad \bar\epsilon = \frac{\epsilon}{L_0} \quad \boldsymbol u(x,t) = \frac{\bar{\boldsymbol u}(\bar{\boldsymbol x},\bar t)}{L_0}. \tag{3.4.6}$$

From above it is easy to see that $\bar S(\bar{\boldsymbol x},\bar{\boldsymbol y},\bar t) = \frac{\bar{\boldsymbol u}(\bar{\boldsymbol y},\bar t)-\bar{\boldsymbol u}(\bar{\boldsymbol x},\bar t)}{|\bar{\boldsymbol y}-\bar{\boldsymbol x}|}\cdot\frac{\bar{\boldsymbol y}-\bar{\boldsymbol x}}{|\bar{\boldsymbol y}-\bar{\boldsymbol x}} = S(\boldsymbol x,\bar{\boldsymbol y},t)$. We write

$$\bar r = \sqrt{|\bar{\boldsymbol x}-\bar{\boldsymbol y}|}\bar S = \sqrt{L_0}\sqrt{|x-y|}S = \sqrt{L_0}r, \tag{3.4.7}$$

where $r = \sqrt{|x-y|}S$. The non-dimensional potential function f is related to $\bar f$ by

$$f(r) = \frac{\bar f(\sqrt{L_0}r)}{L_0\bar\rho v_0^2} = \frac{1}{L_0\bar\rho v_0^2}\bar C(1-\exp[-L_0\bar\beta r^2]). \tag{3.4.8}$$

It is now clear that the dimension of $\bar{f}$ is the same as $L_0\bar{\rho}v_0^2$ and therefore f is non-dimensional. We have,

$$f'(r) = \frac{\bar{f}'(\sqrt{L_0}r)}{\sqrt{L_0}\bar{\rho}v_0^2} = \frac{2\bar{C}\bar{\beta}r}{\bar{\rho}v_0^2}\exp[-L_0\bar{\beta}r^2]. \tag{3.4.9}$$

Collecting results we now see that the peridynamic equation 3.4.4 is equivalent to the non-dimensional equation of motion **??** with density $\rho = 1$, i.e.,

$$\left(\frac{\bar{\rho}v_0^2}{L_0}\right)\partial_{tt}\boldsymbol{u} = \bar{\rho}\partial_{\bar{t}\bar{t}}\bar{\boldsymbol{u}} = \bar{\mathcal{L}}_T^{\bar{\epsilon}}(\bar{\boldsymbol{u}})(\bar{\boldsymbol{x}}) = \left(\frac{\bar{\rho}v_0^2}{L_0}\right)\mathcal{L}_T^{\epsilon}(\boldsymbol{u})(\boldsymbol{x}), \tag{3.4.10}$$

so

$$\partial_{tt}\boldsymbol{u} = \mathcal{L}_T^{\epsilon}(\boldsymbol{u})(\boldsymbol{x}). \tag{3.4.11}$$

3.4.2 Lipschitz continuity constant and bound on error

The exact solution is in $\boldsymbol{u} \in C_0^{0,1}(D;\mathbb{R}^2)$, and the bound on the spatial discretization error becomes,

$$\sup_k e^k \leq \exp\left[T(1 + L_3/\epsilon^2)\right] T(C_s/\epsilon^2)h, \tag{3.4.12}$$

where

$$L_3 = 4C_2^f\bar{J}_1, \quad C_2^f = \sup_r |f''(r)|, \quad \bar{J}_1 = \frac{1}{\omega_2}\int_{H_1(\mathbf{0})} J(|\boldsymbol{\xi}|)/|\boldsymbol{\xi}|d\boldsymbol{\xi}, \quad \omega_2 = \pi$$

and

$$\begin{aligned} C_s &= \sqrt{2L_0}\left[\epsilon^2 \sup_t \left\|\frac{\partial^2\boldsymbol{u}(t)}{\partial t^2}\right\|_{C^{0,\gamma}} + L_3\sup_t \|\boldsymbol{u}(t)\|_{C^{0,\gamma}}\right] \\ &\approx L_3\sqrt{2}\sqrt{L_0}\sup_t \|\boldsymbol{u}(t)\|_{C^{0,\gamma}}, \end{aligned}$$

where we have ignored the order ϵ^2 term.

For $f(r) = \frac{1}{L_0\bar{\rho}v_0^2}\bar{C}(1 - \exp[-L_0\bar{\beta}r^2])$ and $J(r) = a(1-\xi)$, it can be seen that

$$C_2^f = \frac{2\bar{C}\bar{\beta}}{\bar{\rho}v_0^2}, \quad \bar{J}_1 = a. \tag{3.4.13}$$

Now $\bar{C}\bar{\beta} = \bar{\rho}v_0^2$ so

$$L_3 = \frac{8a}{\epsilon^2}. \tag{3.4.14}$$

The upper bound on error is given by

$$\sup_k e^k \leq \sqrt{2L_0}\exp[(1 + \frac{8a}{\epsilon^2})T]T\frac{8a}{\epsilon^2}\sup_t \|\boldsymbol{u}(t)\|_{C^{0,\gamma}}h/\epsilon^2,$$

and the a-priori upper bound on the relative error is denoted by α where

$$\alpha = \sqrt{2L_0}\exp[(1 + \frac{8a}{\epsilon^2})T]8a\frac{Th}{\epsilon^2} \tag{3.4.15}$$

3.4.3 Numerical value of α

We set $L_0 = 1, \epsilon = 1/10, h = 1/100$ and we fix $a = 0.001$ and $v_0 = \sqrt{\frac{\bar{C}\bar{\beta}}{\bar{\rho}}}$. The material properties of plexiglass at room temperature are given by the density $\bar{\rho} = 1200\, kg/m^3$, the bulk modulus $K = 25\, GPa$, and the critical energy release rate $G = 500\, Jm^{-2}$. We then have

$$\alpha = \exp[1.8T]0.012T. \tag{3.4.16}$$

Here the relative error upper bound $\alpha < 1/10$ when the non-dimensional time $T \leq \frac{2}{1.8} = 1.111$. Therefore the actual time in seconds of the simulation can be $\bar{T} = T_0 \times T \leq (L_0/v_0) \times 1.111 = 1.433\mu$s.

3.4.4 Discussion on error accumulation in the numerics

Fracture in notched plexiglass samples can last up to several hundred microseconds. From the previous subsection we see that error increases by factor 1/10 every 1.433μs for nonlinear peridynamic material. This gives us about 5μs of simulation time till the a-priori bound on the relative error is about 1/2. However, from the numerical experiments conducted in the following section we find that the discrete simulation is stable and converges with h at a linear rate for a far longer amount of time than predicted by the a-priori estimates.

To explain this we first note that the region where nonlinearity is strong is always restricted to a very small region, with area $L_0 \times 2\bar{\epsilon}$ in 2-d for a single crack. For points in the region away from the crack the deformation is smooth. In this region the material behaves like a linear elastic material up to a small error of the order of $O(\bar{\epsilon})$. This is shown for this model when the solution is smooth and using [Proposition 6, [Jha and Lipton 2018b] we write

$$\bar{\mathcal{L}}^{\bar{\epsilon}}_T(\bar{\boldsymbol{u}})(\bar{\boldsymbol{x}}) = \nabla \cdot \mathbb{C}\mathcal{E}\bar{\boldsymbol{u}}(\bar{\boldsymbol{x}}) + O(\bar{\epsilon}), \tag{3.4.17}$$

where

$$\mathcal{E}\bar{\boldsymbol{u}}(\bar{\boldsymbol{x}}) = \frac{1}{2}(\nabla\bar{\boldsymbol{u}}(\bar{\boldsymbol{x}}) + \nabla\bar{\boldsymbol{u}}(\bar{\boldsymbol{x}})^T), \tag{3.4.18}$$

$$\mathbb{C}_{ijkl} = 2\mu\frac{\delta_{ik}\delta_{jl} + \delta_{il}\delta_{jk}}{2} + \lambda\delta_{ij}\delta_{kl}, \tag{3.4.19}$$

$$\lambda = \mu = \frac{\bar{f}''(0)}{8}\int_0^1 J(\xi)\xi^2 d\xi = \bar{C}\bar{\beta}\frac{a}{48}, \tag{3.4.20}$$

where last equation is for $d = 2$ and for $J(\xi) = a(1-\xi)$. We now observe that for the non-dimensional function $f(r) = \frac{1}{L_0\bar{\rho}v_0^2}\bar{C}(1 - \exp[-L_0\bar{\beta}r^2])$, $f''(0) = 2$. Using this we can write

$$\bar{\mathcal{L}}^{\bar{\epsilon}}_T(\bar{\boldsymbol{u}})(\bar{\boldsymbol{x}}) = \frac{\bar{C}\bar{\beta}}{L_0}\frac{a}{48}\nabla \cdot \hat{\mathbb{C}}\mathcal{E}\boldsymbol{u}(\boldsymbol{x}) + O(\bar{\epsilon}), \tag{3.4.21}$$

where $\hat{\mathbb{C}}$ is given by Equation 4.2.7 for the choice $\lambda = \mu = 1$.

Substituting Equation 3.4.17 into Equation 3.4.11 we get

$$\bar{\mathcal{L}}^{\bar{\epsilon}}_T(\boldsymbol{u})(\boldsymbol{x}) = \left(\frac{\bar{\rho}\tilde{v}_0^2}{L_0}\right)\nabla \cdot \hat{\mathbb{C}}\mathcal{E}\boldsymbol{u}(\boldsymbol{x}) + O(\bar{\epsilon}), \tag{3.4.22}$$

Parameters \ Poisson's ratio	$\nu = 0.245$	$\nu = 0.25$
c	4712.4	4712.4
C	-1.0623×10^{12}	0
β	1.7533×10^{8}	1.5279×10^{8}
$r* = \frac{1}{\sqrt{2\beta}}$	5.3402×10^{-5}	5.7206×10^{-5}

Table 3.1: Peridynamic material parameters assuming bulk modulus $K = 25\,GPa$ and critical energy release rate $G_c = 500\,J/m^{-2}$. Density is $\rho = 1200\,kg/m^3$.

with

$$\tilde{v}_0 = \sqrt{\frac{\bar{C}\bar{\beta}}{48\bar{\rho}}} = \sqrt{\frac{\lambda}{\bar{\rho}}}. \tag{3.4.23}$$

where we have used the relation Equation 3.4.3 and $\lambda = \mu$ and $\tilde{v}_0$ is the s-wave speed in plexiglass.

It follows from Equation 3.4.22, that for regions where nonlinearity is negligible then the solution should be an approximation to the solution of the linear elastic wave equation. This is shown for smooth solutions in [Theorem 5, [Jha and Lipton 2018b]] so the total error accumulated at each time step is far less than in the nonlinear region. The error due to the truly nonlinear peridynamic interaction is restricted to a region of small area $2L_0\bar{\epsilon}$. This explains why simulations in the next section exhibit a linear rate of convergence in h for a longer time than predicted from the a-priori estimates.

3.5 Numerical results

In this section, we present numerical simulations that support the theoretical upper bound on the convergence rate. We also show the sharp crack propagation in the sample under the bending load. We specify the density $\rho = 1200\,kg/m^3$, bulk modulus $K = 25\,GPa$, and critical energy release rate $G_c = 500\,Jm^{-2}$. The pairwise interaction and the hydrostatic interaction are characterized by potentials $f(r) = c(1 - \exp[-\beta r^2])$ and $g(r) = Cr^2/2$ respectively. The influence function is $J(r) = 1 - r$. We present results when hydrostatic force is active (when Poisson's ratio $\nu = 0.245$) and when hydrostatic force is inactive (when $\nu = 0.25$). Equations 94, 95, and 97 of [Lipton et al., 2018b] relate parameters c, β, C to the Lamè parameters λ, μ and the critical energy release rate G_c. In Table 3.1 we list the values of parameters. The critical bond strain between material point $\boldsymbol{y}$ and $\boldsymbol{x}$ is $S_c = r^*/\sqrt{|\boldsymbol{y} - \boldsymbol{x}|}$ where $r^* = 1/\sqrt{2\beta}$.

We consider the central difference time discretization described by Equation 3.3.10 and Equation 3.3.11 on a uniform square mesh of mesh size h. We can write the peridynamic force $\mathcal{L}^\epsilon(\hat{\boldsymbol{u}}^k)(\boldsymbol{x}_i)$ as follows

$$\mathcal{L}^\epsilon(\hat{\boldsymbol{u}}^k)(\boldsymbol{x}_i) = \int_{H_\epsilon(\boldsymbol{x}_i)} (w_1(\boldsymbol{y}, \boldsymbol{x}_i) + w_2(\boldsymbol{y}, \boldsymbol{x}_i))d\boldsymbol{y}, \tag{3.5.1}$$

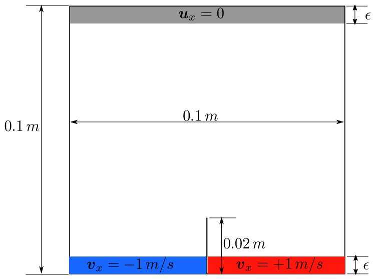

Figure 3.2: Material domain $D = [0, 0.1\,m]^2$ with crack of length $0.02\,m$. The x-component of displacement is fixed along a collar of thickness equal to the horizon on top. On the bottom the velocity $\boldsymbol{v}_x = \pm 1\,m/s$ along x-direction is specified on either side of the crack to make the crack propagate upwards.

where w_1 and w_2 can be determined from expression of $\mathcal{L}^\epsilon$ in Equation 1.2.12. In the simulation we approximate $\mathcal{L}^\epsilon(\hat{\boldsymbol{u}}^k)(\boldsymbol{x}_i)$ as below

$$\mathcal{L}^\epsilon(\hat{\boldsymbol{u}}^k)(\boldsymbol{x}_i) \approx \sum_{\boldsymbol{x}_j \in D_h \cap H_\epsilon(\boldsymbol{x}_i)} (w_1(\boldsymbol{x}_j, \boldsymbol{x}_i) + w_w(\boldsymbol{x}_j, \boldsymbol{x}_i)) V_j \bar{V}_{ij}, \tag{3.5.2}$$

where $V_j = h^2$ for uniform mesh in 2-d and $\bar{V}_{ij}$ is the volume correction. The correction is the ratio of the volume of the mesh element contained within the horizon of $\boldsymbol{x}_i$ and the volume V_j. The numerical results are presented in the following section.

3.5.1 Crack propagation: Fracture energy and numerical convergence study

We consider a 2-d domain $D = [0, 0.1\,m]^2$ (with unit thickness in the third direction) with a vertical pre-crack of length $0.02\,m$. We use a uniform square mesh of size h. The boundary conditions are described in Figure 3.2. The simulation time is $T = 34\,\mu s$ and the time step is $\Delta t = 0.004\,\mu s$. In what follows we run the simulations for three different horizons $\epsilon = 8\,mm, 4\,mm, 2\,mm$. For the coarsest horizon $\epsilon = 8\,mm$, the number of mesh nodes are (approximately) $0.9 \times 10^3, 3.5 \times 10^3, 13.7 \times 10^3$ for $h = 4, 2, 1\,mm$ respectively. The memory consumed are 10 MB, 16 MB, 95 MB respectively. For the finest horizon, $\epsilon = 2\,mm$, the number of nodes is $11 \times 10^3, 44 \times 10^3, 174 \times 10^3$ for $h = 1, 0.5, 0.25\,mm$ respectively. The memory consumed are 16.4 MB, 99.4 MB, 1126.4 MB respectively. All computations were performed on a single workstation in parallel using 20 threads.

Fracture energy of crack zone

The extent of damage at a material point $\boldsymbol{x}$ is given by the function $Z(\boldsymbol{x})$

$$Z(\boldsymbol{x}) = \max_{\boldsymbol{y} \in H_\epsilon(\boldsymbol{x}) \cap D} \frac{S(\boldsymbol{y}, \boldsymbol{x}; \boldsymbol{u})}{S_c}. \tag{3.5.3}$$

We define the crack zone as the set of material points which have $Z > 1$. We compute the peridynamic energy of crack zone and compare it with the Griffith's fracture energy.

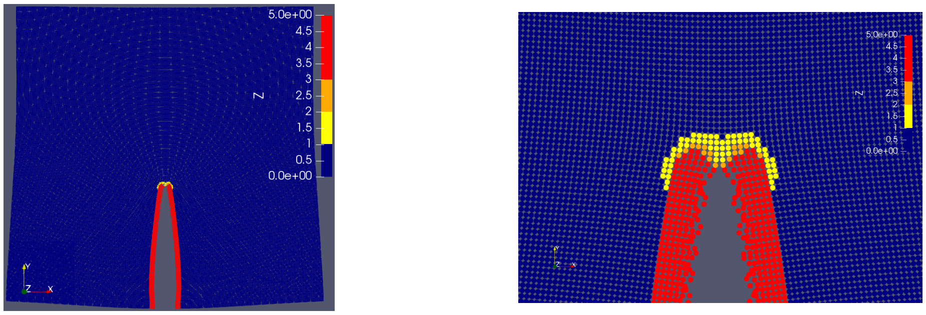

(a) (b)

Figure 3.3: (a) Color plot of damage function Z on deformed material domain at time $t = 34\,\mu s$. Dark blue represents undamaged material $Z < 1$, $Z \approx 1$ is yellow at crack tip, red is softening material. The plot is for a horizon $\epsilon = 2\,mm$ and $h = \epsilon/8$. Here, the displacements are scaled by 100 and damage function is cut off at 5 to highlight the crack zone. The maximum displacement is $4.4\,mm$ and the maximum value of $Z(x)$ is 82 at $t = 34\,\mu s$. (b) View near the crack tip.

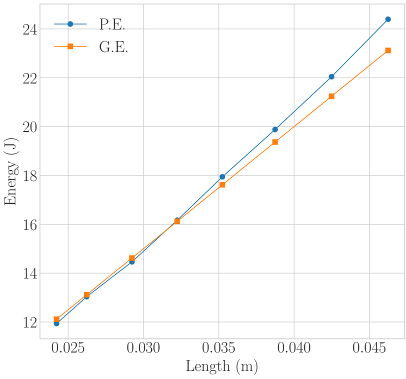

Figure 3.4: Crack length vs peridynamic fracture energy (P.E.) and Griffith's fracture energy (G.E.). G.E. is simply $G_c \times l$ where $G_c = 500$. Plot is for $\epsilon = 2\,mm$.

For a crack of length l, the Griffith's fracture energy (G.E.) will be $G.E. = G_c \times l$. The peridynamic fracture energy (P.E.) is given by

$$P.E. = \int_{\substack{\boldsymbol{x}\in D,\\ Z(\boldsymbol{x})\geq 1}} \left[\frac{1}{\epsilon^d \omega_d} \int_{H_\epsilon(\boldsymbol{x})} |\boldsymbol{y}-\boldsymbol{x}| \mathcal{W}^\epsilon(S(\boldsymbol{y},\boldsymbol{x},\boldsymbol{u}))\, d\boldsymbol{y} \right] d\boldsymbol{x},$$

where $\mathcal{W}^\epsilon(S(\boldsymbol{y},\boldsymbol{x},\boldsymbol{u}))$ is the bond-based potential. For the choice of $f(r)$ and $g(r)$, only bond-based potential f contributes to the fracture energy, therefore $P.E.$ is computed only from bond-based interaction.

Figure 3.3 shows the plot of Z at time $t = 34\,\mu s$ for horizon $\epsilon = 2\,mm$. The figure on the right shows the Z field near a crack tip. In Figure 3.4 we plot the peridynamic and Griffith's fracture energy as a function of crack length. The absolute error between the peridynamic and Griffith's fracture energy remain below 5% for simulation time upto $34\,\mu s$.

Convergence rate

Consider a fixed horizon ϵ and three different mesh sizes $h_1 = \epsilon/2, h_2 = \epsilon/4, h_3 = \epsilon/8$. We compute the convergence rate as follows. Let $\boldsymbol{u}_1, \boldsymbol{u}_2, \boldsymbol{u}_3$ be approximate solutions corresponding to meshes of size h_1, h_2, h_3, and let $\boldsymbol{u}$ be the exact solution. We suppose for $h' < h$ that $\underline{C}h^\alpha \leq ||\boldsymbol{u}_h - \boldsymbol{u}_{h'}|| = \overline{C}h^\alpha$ with $\underline{C} \leq \overline{C}$ and $\alpha > 0$, and fix the ratio of mesh size $h_1/h_2 = h_2/h_3 = r$. A straight forward calculation gives

$$\alpha \leq \frac{\log(||\boldsymbol{u}_1 - \boldsymbol{u}_2||) - \log(||\boldsymbol{u}_2 - \boldsymbol{u}_3||) + \log(\overline{C}) - \log(\underline{C})}{\log(r)}, \tag{3.5.4}$$

so an upper bound on the convergence rate is at least as big as

$$b = \frac{\log(||\boldsymbol{u}_1 - \boldsymbol{u}_2||) - \log(||\boldsymbol{u}_2 - \boldsymbol{u}_3||)}{\log(r)}. \tag{3.5.5}$$

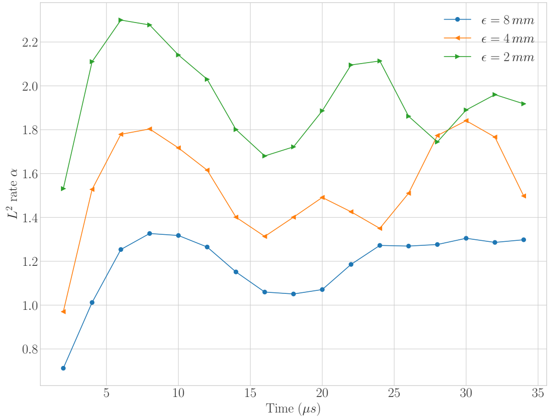

Figure 3.5: Convergence rate with respect to mesh size for different fixed size of horizons.

We calculate the convergence rate estimate b for mesh sizes $h = \epsilon/2, \epsilon/4, \epsilon/8$ and plot it for every $2\mu s$ for times up to $34\mu s$, see Figure 3.5. It is seen that the convergence rate is at least 1 up to the final time of $34\mu s$. These numerical results show a convergence at a rate that is at least as good as the linear a-priori convergence rate obtained in Theorem 3.3.3.

3.5.2 Bending test with pre-crack

We consider a 2-d material domain (with unit thickness in third direction) $D = [0, 0.25\,m] \times [0, 0.05\,m]$ with single and double vertical cracks. We fix horizon to $\epsilon = 0.75\,mm$ and mesh size $h = 0.25\,mm$. The boundary conditions are described in Figure 3.6 for single crack. For the double crack problem, the two vertical cracks are symmetrically located at distance $0.02\,m$ along x-axis from the mid point $x = 0.125\,m, y = 0$. With time step $\Delta t = 0.0035\,\mu s$ we run simulations upto time $T = 350\,\mu s$. Material properties correspond to the Poisson's ration $\nu = 0.25$, see Table 3.1.

In Figure 3.7 we plot the fracture energy as a function of total crack length. The error in energy remain below 5% till $220.5\,\mu s$ for single crack problem and $245\,\mu s$ for double crack problem. In Figure 3.8 damage profile at various times are shown for both single and double crack problem.

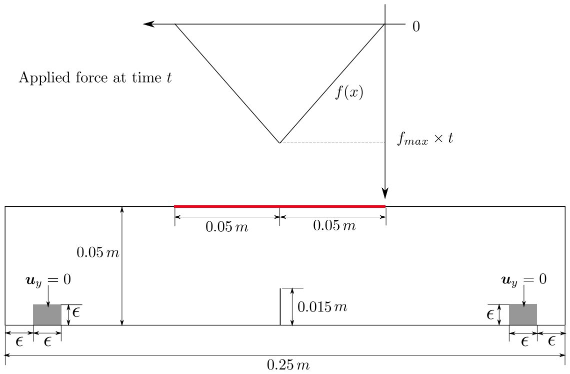

Figure 3.6: Material domain $D = [0, 0.25\,m] \times [0, 0.05\,m]$ with single verticle crack of length $0.015\,m$ at mid point of bottom edge. We apply linear in time distributed load, along negative y-direction, on part of the top edge. At any time t, the load is zero at the end points of loading line (red line) and is $f_{max} \times t$ at the midpoint. We take constant $f_{max} = -2.5 \times 10^{14}$. We fix a vertical displacement on two support regions shown in the figure. Horizon is $\epsilon = 0.75\,mm$.

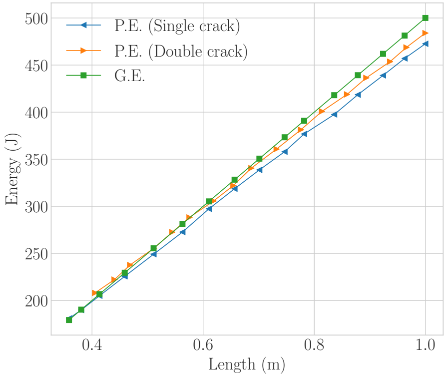

Figure 3.7: Crack length vs peridynamic fracture energy (P.E.) and Griffith's fracture energy (G.E.). Here crack length and fracture energy of single crack and double crack are normalized by crack length $L = 0.038604\,m$ at time $t = 220.5\,\mu s$ and crack length $L = 0.0706034\,m$ at time $t = 245\,\mu s$ respectively.

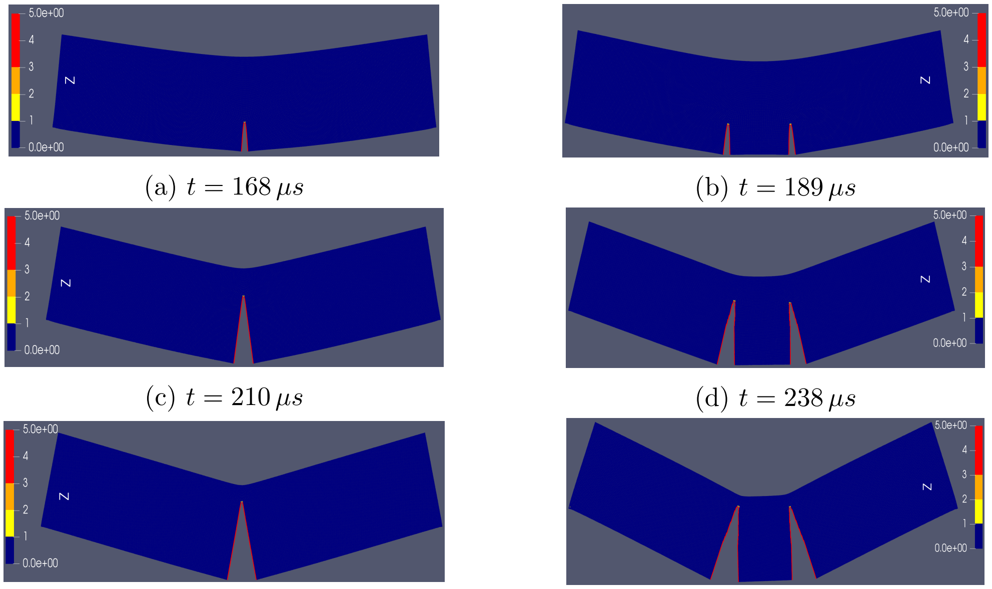

(a) $t = 168\,\mu s$ (b) $t = 189\,\mu s$

(c) $t = 210\,\mu s$ (d) $t = 238\,\mu s$

(e) $t = 224\,\mu s$ (f) $t = 266\,\mu s$

Figure 3.8: Damage profile under bending load. Plots on left are for single crack and plots on right are for double crack.

3.6 Concluding remarks on the finite difference method for nonlocal fracture modeling

In this project, we present an a-priori convergence analysis for a class of nonlinear nonlocal state based peridynamic models. We have shown that the convergence rate applies, even when the fields do not have well-defined spatial derivatives. The results are valid for two different classes of state-based peridynamic models depending on the potential functions associated with the dilatational energy. For both models the potential function characterizing the energy due to tensile strain is of convex-concave type while the potential function for the dilatational strain can be either convex-concave or quadratic. The convergence rate of the discrete approximation to the true solution in the mean square norm is given by $C(\Delta t + h^\gamma/\epsilon^2)$. Here the constant depends on the Hölder and L^2 norm of the true solution and its time derivatives. The Lipschitz property of the nonlocal, nonlinear force together with boundedness of the nonlocal kernel plays an important role. It ensures that the error in the nonlocal force remains bounded when replacing the exact solution with its approximation. This, in turn, implies that even in the presence of mechanical instabilities the global approximation error remains controlled by the local truncation error in space and time. We have described the connection between the non-dimensionalized dynamics used in the a-priori convergence analysis and the simulated dynamics using dimensional quantities. The numerics are carried out for plexiglass. The a-priori estimates predict a simulation time of a few microseconds before the relative error grows too large. On the other hand the numerical simulation with crack propagation looks to be stable and one can control the error by choosing the time step and spatial discretization sufficiently small. The simulation shows a linear convergence rate with respect to mesh size for simulation times ten times larger than predicted by the a-priori estimates. This is due to the fact that the nonlinearity is isolated on a set of small area related to the crack set. Away from the crack set the evolution is linearly elastic and characterized by the shear wave speed of plexiglass. This observation motivates future work that will address a-posteriori error estimation and mesh adaptivity.

Chapter 4

Convergence of the cohesive nonlocal fracture model to linear elastic fracture mechanics

4.1 Introduction

The appeal of nonlocal fracture models is that cracks appear as emergent phenomena generated by the underlying field theory eliminating the need for supplemental kinetic relations describing crack growth. As outlined earlier the deformation field inside the body for points $\boldsymbol{x}$ at time t is written $\boldsymbol{u}(\boldsymbol{x}, t)$ and the model is described simply by the balance of linear momentum of the form

$$\rho \boldsymbol{u}_{tt}(\boldsymbol{x}, t) = \int_{\mathcal{H}_\epsilon(\boldsymbol{x})} \boldsymbol{f}(\boldsymbol{y}, \boldsymbol{x}) \, d\boldsymbol{y} + \boldsymbol{b}(\boldsymbol{x}, t). \tag{4.1.1}$$

Here $\mathcal{H}_{\epsilon(\boldsymbol{x})}$ is a neighborhood of $\boldsymbol{x}$, ρ is the density, $\boldsymbol{b}$ is the body force density field, and $\boldsymbol{f}$ is the material-dependent constitutive law that represents the force density that a point $\boldsymbol{y}$ inside the neighborhood exerts on $\boldsymbol{x}$ as a result of the deformation field. The radius ϵ of the neighborhood is referred to as the *horizon*. Here all points satisfy the same basic field equations (4.1.1). In this project we examine the displacement fields and fracture evolution predicted by nonlocal models. In order to be a valid theory the predictions of the nonlocal models must agree with those of modern fracture mechanics. Our theoretically based investigation indicates that certain classes of nonlocal models will *agree* with the established theory of dynamic fracture mechanics when the length scale of non-locality is sufficiently small. Unfortunately we are not able to give a rate of convergence for the non-locally based fracture evolution to the Linear Elastic Fracture Mechanics LEFM based evolution. On the other hand we can establish using applied mathematics that LEFM is the target theory for the nonlocal model when the length scale of non-locality tends to zero. At this time the same question is wide open for other nonlocal dynamic approaches including the phase field numerical approach, XFEM, and the level set approaches. One conjectures that it should be true for the correct formulation of these models and this is a goal for future work. This requirement is absolute and can be used to rule out proposed heuristic regularizations of LFEM whose target theory is subsequently determined not to be LFEM.

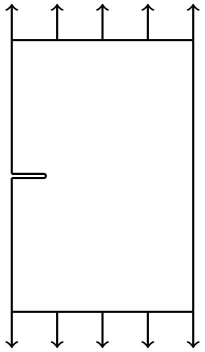

Figure 4.1: **Single-edge-notch**

In this project we theoretically examine the predictions of the nonlocal theory in the limit of vanishing non-locality. We examine a class of peridynamic models with nonlocal forces derived from double well potentials. see [Lipton, 2014], [Lipton, 2016]. We investigate the limit of these evolutions as the length scale ϵ of nonlocal interaction goes to zero. We are able to describe the interaction between the crack and the surrounding displacement field of intact material in this limit. Here all information on this limit is obtained from what is known from the nonlocal peridynamic model for $\epsilon > 0$. We consider a single edge notch specimen as given in Figure 4.1. For small strains the nonlocal force is linearly elastic but for larger strains the force begins to soften and then approaches zero after reaching a critical strain. Because of this force vs. strain behavior this type of model is called a cohesive model.

Previous work has addressed the convergence of the cohesive fracture model to classic local brittle fracture for dynamic free crack propagation with multiple interacting cracks [Lipton, 2014], [Lipton, 2016], [Jha and Lipton, 2018a]. There it is shown that the nonlocal cohesive evolution converges to an evolution of sharp cracks with bounded Griffith fracture energy satisfying the linear elastic wave equation off the cracks. However the explicit interaction between the sharp crack and intact material remains to be described in the local limit. In this work we describe in an explicit way the limiting interaction between the sharp crack and surrounding material. Here we pass to the limit in the nonlocal model to recover the limiting dynamic interaction of the sharp crack with the surrounding intact material. A distinguishing feature of the cohesive nonlocal model is that the fracture toughness is the same for all horizons $\epsilon > 0$. It is shown here that fracture evolutions are mathematically well posed for every $\epsilon > 0$ and that as $\epsilon \to 0$ the nonlocal evolution converges to the dynamic brittle fracture model given by:

- Balance of linear momentum described by the linear elastic wave equation away from the crack.
- Zero traction on the crack lips.
- The classic kinetic relation for crack tip velocity implicitly given by equating the dynamic stress intensity factor with the energy dissipation per unit extension of the crack.

However in this project the kinetic relation for crack tip velocity is *not derived from the power balance postulate of* [Mott, 1948] but instead is recovered from the nonlocal model

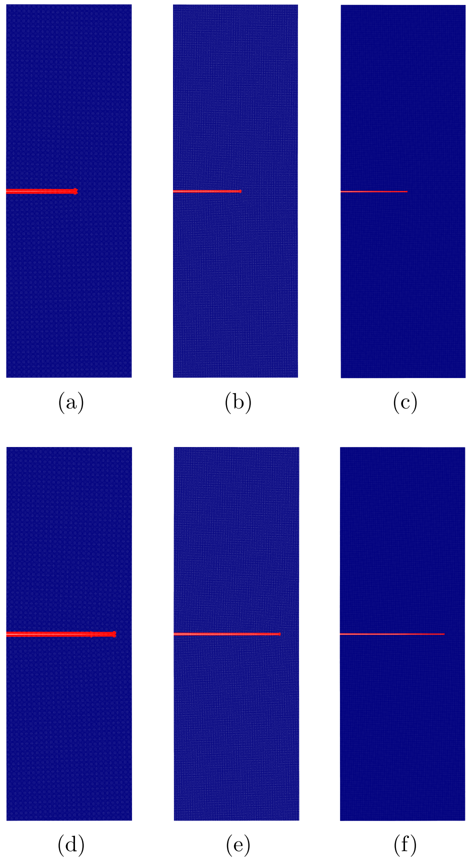

Figure 4.2: **Using the nonlocal model the crack is captured as softening zone (red) for different horizons. (a), (b), (c) at $t = 460\,\mu$s for $\epsilon = 2.5, 1.25, 0.625$ mm. (d), (e), (f) correspond to softening zone $t = 520\,\mu$s for $\epsilon = 2.5, 1.25, 0.625$ mm.**

(1.2.11) directly by taking the $\epsilon = 0$ limit in the nonlocal power balance, see the following section. The kinetic relation derived here follows from an explicit formula for the time rate of change of internal energy inside a domain containing the crack tip. In this way we recover the modern dynamic fracture model developed and described in [Freund, 1998], but without using the power balance postulate. Instead the rate of internal energy increase in a neighborhood surrounding the advancing defect in the nonlocal formulation is calculated directly. This can be done since the field theory in the vicinity of the advancing defect is well defined for the nonlocal model. It is shown analytically that the change in internal energy converges to the well known difference between fracture energy and elastic energy flowing into the crack tip in the limit of vanishing nonlocality. We note further that the limiting classic local fracture problem is hard to simulate directly, this is because the crack velocity at the crack tip is directly coupled to the wave equation off the crack and vice versa. On the other hand this coupling between intact material and crack is handled autonomously in the nonlocal model and numerical simulation is straight forward.

We numerically simulate the single edge notch in tension using the nonlocal model for progressively smaller nonlocal interaction in Figures 4.2 and 4.3. The softening zone becomes thinner and more localized to the $x_2 = 0$ axis as the length scale of the nonlocal

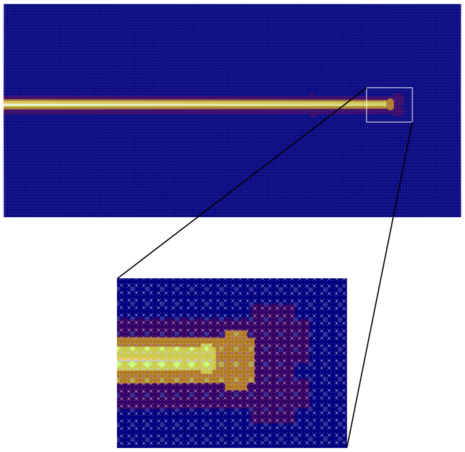

Figure 4.3: **Top: Softening zone for $\epsilon = 2.5, 1.25, 0.625$ mm at time $t = 520\,\mu$s on top of each other. Red, light yellow, and light blue color is used for softening zone of horizon $2.5, 1.25, 0.625$ mm respectively. Bottom: Zoomed in near the tip**.

interaction decreases approaching a crack. This is corroborated theoretically. The tip of the softening zone emerges from our simulations and in Figure 4.4 we plot the tip of the softening zone (x-coordinate) at different times. We see that softening zone tip for the larger horizon is consistently ahead of the crack tip for the smaller horizon.

The analysis used in this project relies in part on the earlier analysis of [Lipton, 2016] but also requires new compactness methods specifically suited to the balance of momentum for nonlocal - nonlinear operators. The interaction between crack tip and intact material for the nonlocal model delivers the kinetic relation for LEFM in the $\epsilon \to 0$ limit, this is highlighted in the next section.

These results have been archived in the preprint [Lipton and Jha, 2019] and are being prepared for journal publication as two separate articles.

4.2 Crack tip interaction with intact material and the kinetic relation for LEFM

We address crack tip interaction with intact elastic material by calculating the limiting change in internal energy inside a neighborhood enclosing the defect tip for the nonlocal model as the length scale of nonlocal interaction $\epsilon \to 0$. For a nonlocal evolution with perydynamic horizon ϵ consider the rectangular contour $\Gamma^\epsilon_\delta(t)$ of diameter δ surrounding the domain $\mathcal{P}^\epsilon_\delta(t)$ containing the crack tip, see Figure 4.5. We suppose $\mathcal{P}^\epsilon_\delta(t)$ is moving with the crack tip velocity $V^\epsilon(t)\boldsymbol{e}^1$ where the unit vector $\boldsymbol{e}^1$ is along the horizontal axis. To fix ideas we assume that the force due to volume change is small and that the potential energy is given exclusively by (1.2.2). Define the kinetic energy density by $T^\epsilon = \rho|\boldsymbol{u}^\epsilon(\boldsymbol{x},t)|^2/2$ and the nonlocal potential energy density is given by $W^\epsilon(\boldsymbol{x}) = \int_{\mathcal{H}_\epsilon(\boldsymbol{x})} |\boldsymbol{y}-\boldsymbol{x}|\mathcal{W}^\epsilon(S(\boldsymbol{y},\boldsymbol{x},\boldsymbol{u}^\epsilon(t)))\,d\boldsymbol{y}$.

The the rate of change of internal energy inside the domain containing the defect tip is given explicitly by

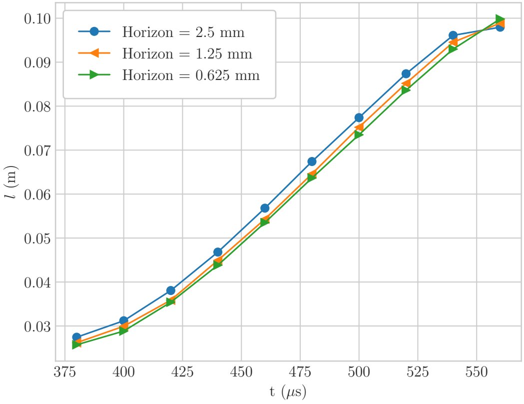

Figure 4.4: **The softening zone length is plotted as a function of time for three different horizons.**

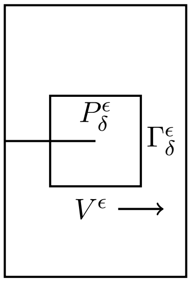

Figure 4.5: **Contour Γ_δ^ϵ surrounding the domain P_δ^ϵ moving with the defect tip velocity V^ϵ.**

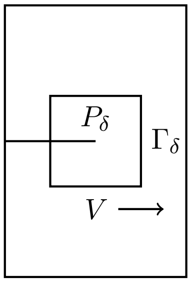

Figure 4.6: **Contour Γ_δ surrounding the domain P_δ moving with the velocity V of the crack centerline.**

Proposition 4.2.1

$$\frac{d}{dt}\int_{\mathcal{P}^\epsilon_\delta(t)} T^\epsilon + W^\epsilon \, d\boldsymbol{x} = I^\epsilon(\Gamma^\varepsilon_\delta(t)) \tag{4.2.1}$$

with

$$I^\epsilon(\Gamma^\varepsilon_\delta(t)) = \int_{\Gamma^\epsilon_\delta(t)} (T^{\epsilon_n} + W^{\epsilon_n}) V^{\epsilon_n} \boldsymbol{e}^1 \cdot \boldsymbol{n} \, ds - E^{\epsilon_n}(\Gamma^{\epsilon_n}_\delta(t)), \tag{4.2.2}$$

and

$$\begin{aligned} &E^{\epsilon_n}(\Gamma^{\epsilon_n}_\delta(t)) \\ &= \int_{A^{\epsilon_n}_\delta(t)} \int_{\mathcal{H}_{\epsilon_n}(\boldsymbol{x})\cap \mathcal{P}^{\epsilon_n}_\delta(t)} \partial_S \mathcal{W}^{\epsilon_n}(S(\boldsymbol{y},\boldsymbol{x},\boldsymbol{u}^{\epsilon_n}))\boldsymbol{e}_{\boldsymbol{y}-\boldsymbol{x}} \cdot (\dot{\boldsymbol{u}}^{\epsilon_n}(\boldsymbol{x}) + \dot{\boldsymbol{u}}^{\epsilon_n}(\boldsymbol{y}))\, d\boldsymbol{y} d\boldsymbol{x}, \end{aligned}$$

where $\boldsymbol{n}$ is the unit normal pointing out of the domain $\mathcal{P}^{\epsilon_n}_\delta(t)$ and $A^{\epsilon_n}_\delta(t)$ is the part of D exterior to $\mathcal{P}^{\epsilon_n}_\delta(t)$.

As $\epsilon \to 0$ the contour $\Gamma^\epsilon_\delta(t)$ converges to $\Gamma_\delta(t)$ of diameter surrounding the domain $\mathcal{P}_\delta(t)$ containing the crack tip for the local model, see Figure 4.6. This domain is moving to the right with the crack tip velocity V. On passing to the $\epsilon \to 0$ limit in the nonlocal cohesive model the rate of change of internal energy inside P_δ can be explicitly calculated and is given by

$$\lim_{\epsilon\to 0}\frac{d}{dt}\int_{\mathcal{P}_\delta(t)} T^\epsilon + W^\epsilon \, d\boldsymbol{x} = \int_{\Gamma_\delta(t)} \mathbb{C}\mathcal{E}\boldsymbol{u}^0\boldsymbol{n}\cdot\dot{\boldsymbol{u}}^0\, ds - \mathcal{G}_c V(t) + O(\delta), \tag{4.2.3}$$

where T^ϵ is the kinetic energy density and W^ϵ is the energy density given by

$$W^\epsilon(\boldsymbol{x},t) = \int_{\mathcal{H}_\epsilon(\boldsymbol{x})\cap D} |\boldsymbol{y}-\boldsymbol{x}| \mathcal{W}^\epsilon(S(\boldsymbol{y},\boldsymbol{x},\boldsymbol{u}^\epsilon(t)))\, d\boldsymbol{y}, \tag{4.2.4}$$

The fracture toughness and elastic tensor are obtained directly from the nonlocal potential. The fracture toughness is given by

$$\mathcal{G}_c = 2\int_0^\epsilon \int_z^\epsilon \int_0^{\arccos(z/\zeta)} \mathcal{W}^\epsilon(\mathcal{S}^+_c)\zeta^2 \, d\psi\, d\zeta\, dz \tag{4.2.5}$$

where $\zeta = |\boldsymbol{y}-\boldsymbol{x}|$, see Figure 4.7. Substitution of $\mathcal{W}^\epsilon(S(\boldsymbol{y},\boldsymbol{x},\boldsymbol{u}(t)))$ into (4.2.5) and calculation delivers the explicit formula for the fracture toughness

$$\mathcal{G}_c = \frac{4}{\pi}\int_0^1 f(S^+_c) r^2 J(r) dr. \tag{4.2.6}$$

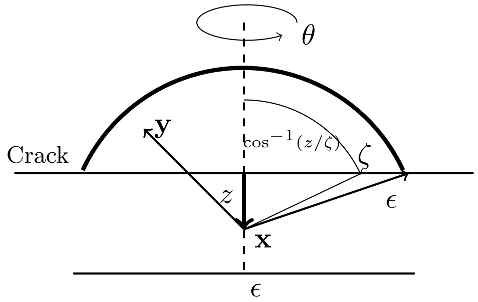

Figure 4.7: **Evaluation of fracture toughness $\mathcal{G}_c$. For each point $\boldsymbol{x}$ along the dashed line, $0 \leq z \leq \epsilon$, the work required to break the interaction between $\boldsymbol{x}$ and $\boldsymbol{y}$ in the spherical cap is summed up in** (4.2.5) **using spherical coordinates centered at $\boldsymbol{x}$.**

and the elastic tensor is given by

$$\mathbb{C}_{ijkl} = 2\mu\left(\frac{\delta_{ik}\delta_{jl} + \delta_{il}\delta_{jk}}{2}\right) + \lambda\delta_{ij}\delta_{kl}, \tag{4.2.7}$$

with shear modulus μ and Lamé coefficient λ given by

$$\mu = \frac{f''(0)}{10}\int_0^1 r^3 J(r)\,dr \text{ and } \lambda = \frac{f''(0)}{10}\int_0^1 r^3 J(r)\,dr. \tag{4.2.8}$$

If the limit of the internal energy is not changing in time then in the $\delta = 0$ limit we recover the power balance for the local model given by

$$V(t)\mathcal{G}_c = J = \lim_{\delta \to 0} J_\delta, \tag{4.2.9}$$

where J_δ is the rate of energy flowing into $\mathcal{P}_\delta(t)$ towards the crack tip for the local model given by

$$J_\delta = \int_{\Gamma_\delta} \mathbb{C}\mathcal{E}\boldsymbol{u}^0\boldsymbol{n} \cdot \dot{\boldsymbol{u}}^0\,ds. \tag{4.2.10}$$

This well known situation can happen for cracks propagating at constant velocity inside domains with remote boundaries [Freund and Clifton(1974)]. Here $\boldsymbol{n}$ is the outward directed unit normal, ds is an element of arc length and $\mathbb{C}\mathcal{E}\boldsymbol{u}^0 : \mathcal{E}\boldsymbol{u}^0$ is the elastic energy density. Clearly the crack advances if $J > 0$. The formula recovered in this project is in the form given by [Freund and Clifton(1974)]. Based on the nature of the dynamic stress field [Atkinson and Eshelby(1968)], [Kostrov and Nikitin(1970)], [Freund(1972)], and [Willis(1975)] provide a representation of the instantaneous rate of energy flowing into the crack tip, is given by

$$J = \frac{1+\nu}{E}\frac{V^3}{c_s^2 D}\alpha_t K_I^2(t), \tag{4.2.11}$$

were ν is the Poisson ratio, E is the Young modulus V is the crack velocity, c_s is the shear wave speed, $c_l = (\lambda + 2\mu/\rho)^{1/2}$ is the longitudinal wave speed, $D = 4\alpha_s\alpha_l - (1+\alpha_s^2)^2$, and $\alpha_s = (1 - V^2/c_s^2)^{1/2}$, $\alpha_l = (1 - V^2/c_l^2)^{1/2}$. Here $K_I(t)$ is the mode I dynamic stress intensity factor and depends on the details of the loading and is not explicit. On applying Equation 4.2.9 we recover the kinetic relation for the crack tip velocity given by

$$\mathcal{G}_c = \frac{J}{V} = \frac{1+\nu}{E}\frac{V^2}{c_s^2 D}\alpha_t K_I^2(t), \tag{4.2.12}$$

see [Freund, 1998]. In this way the nonlocal model recovers the LEFM kinetic relation for crack tip motion in the limit of vanishing horizon.

4.3 Concluding remarks

In this project we demonstrate that the nonlocal cohesive model has solutions that converge in the limit of vanishing non-locality to classic plane elastodynamics with a running crack. The normal traction on the crack lips is zero and the energy release rate given by the generalized Irwin relationship ([Freund, 1998], equation (5.39)). The kinetic relation for crack tip motion corresponds to a zero change in internal energy inside domains containing the crack tip and is the classic one given by (4.2.12). The power balance given by (4.2.9) is not postulated but instead recovered by taking the $\epsilon = 0$ limit in the nonlocal power balance. In this way one sees that the generalized Irwin relationship is a consequence of the nonlocal cohesive dynamics in the $\epsilon_n = 0$ limit. The recovery is possible since the nonlocal model is well defined over "the process zone" around the tip of the softening region. This shows that the double well potential provides a phenomenological description of the process zone at mesoscopic length scales.

The ideas have been illustrated using the simplest double well energy for a bond based perydynamic formulation. We are free to take a more sophisticated energy like those motivated by the Lennard Jones potential. Doing so will deliver a nonlocal model that preserves non-interpenetration of material points for all types of loadings. We can then pass to the small horizon limit in such a model to recover a sharp fracture model with crack lips that do not interpenetrate. More generally we may consider state based peridynamic models and perform similar analyses. These are projects for the future but we believe that all are theoretically accessible.

Bibliography

[Agwai et al., 2011] Agwai, A., Guven, I., and Madenci, E. (2011). Predicting crack propagation with peridynamics: a comparative study. *International journal of fracture*, 171(1):65–78.

[Aksoylu and Unlu, 2014] Aksoylu, B. and Unlu, Z. (2014). Conditioning analysis of nonlocal integral operators in fractional sobolev spaces. *SIAM Journal on Numerical Analysis*, 52:653–677.

[Atkinson and Eshelby(1968)] Atkinson, C. and Eshelby, J. D. 1968. The flow of energy into the tip of a moving crack. Int. J. Fract. 4, 3–8.

[Bobaru and Hu, 2012] Bobaru, F. and Hu, W. (2012). The meaning, selection, and use of the peridynamic horizon and its relation to crack branching in brittle materials. *International journal of fracture*, 176(2):215–222.

[Bobaru et al., 2016] Bobaru, F., Foster, J. T., Geubelle, P. H., Geubelle, P. H., and Silling, S. A. (2016). Handbook of peridynamic modeling.

[Brenner and Scott, 2007] Brenner, S. and Scott, R. (2007). The mathematical theory of finite element methods, volume 15. *Springer Science & Business Media*, 3 edition.

[Brezis, 1983] Brezis, H. (1983). Analyse fonctionnelle, théorie et application.

[Chen and Gunzburger, 2011] Chen, X. and Gunzburger, M. (2011). Continuous and discontinuous finite element methods for a peridynamics model of mechanics. *Computer Methods in Applied Mechanics and Engineering*, 200(9):1237–1250.

[Demengel, 2012] Demengel, F. (2012). Functional Spaces for the Theory of Elliptic Partial Differential Equations. *Universitext. Springer-Verlag London*, 1 edition.

[Du, 2018a] Du, Q. (2018a). An invitation to nonlocal modeling, analysis and computation. *Proc. Int. Cong. of Math 2018*, Rio de Janeiro, Vol. 3 (3523-3552).

[Du, 2018b] Du, Q. (2018b). Nonlocal modeling, analysis and computation. NSF-CBMS Monograph, SIAM Philadelphia (2018).

[Du et al., 2013a] Du, Q., Gunzburger, M., Lehoucq, R., and Zhou, K. (2013a). Analysis of the volume-constrained peridynamic navier equation of linear elasticity. *Journal of Elasticity*, 113(2):193–217.

[Du et al., 2013b] Du, Q., Ju, L., Tian, L., and Zhou, K. (2013b). A posteriori error analysis of finite element method for linear nonlocal diffusion and peridynamic models. *Mathematics of computation*, 82(284):1889–1922.

[Du et al., 2013c] Du, Q., Tian, L., and Zhao, X. (2013c). A convergent adaptive finite element algorithm for nonlocal diffusion and peridynamic models. *SIAM Journal on Numerical Analysis*, 51(2):1211–1234.

[Emmrich et al., 2013] Emmrich, E., Lehoucq, R. B., and Puhst, D. (2013). Peridynamics: a nonlocal continuum theory. In *Meshfree Methods for Partial Differential Equations VI*, pages 45–65. Springer.

[Foster et al., 2011] Foster, J. T., Silling, S. A., and Chen, W. (2011). An energy based failure criterion for use with peridynamic states. *International Journal for Multiscale Computational Engineering*, 9(6).

[Freund, 1998] Freund, L.,B. (1998). Dynamic Fracture Mechanics. Cambridge University Press, Cambridge, UK., 1998.

[Freund(1972)] Freund, L. B., 1972. Energy flux into the tip of an extending crack in an elastic solid. J. Elasticity 2, 341–349.

[Freund and Clifton(1974)] Freund, B. and Clifton, R J., 1974. On the uniqueness of plane elastodynamic solutions for running cracks. Journal of Elasticity 4, 293–299.

[Gerstle et al., 2007] Gerstle, W., Sau, N., and Silling, S. (2007). Peridynamic modeling of concrete structures. *Nuclear engineering and design*, 237(12):1250–1258.

[Ghajari et al., 2014] Ghajari, M., Iannucci, L., and Curtis, P. (2014). A peridynamic material model for the analysis of dynamic crack propagation in orthotropic media. *Computer Methods in Applied Mechanics and Engineering*, 276:431–452.

[Guan and Gunzburger, 2015] Guan, Q. and Gunzburger, M. (2015). Stability and accuracy of time-stepping schemes and dispersion relations for a nonlocal wave equation. *Numerical Methods for Partial Differential Equations*, 31(2):500–516.

[Ha and Bobaru, 2010] Ha, Y. D. and Bobaru, F. (2010). Studies of dynamic crack propagation and crack branching with peridynamics. *International Journal of Fracture*, 162(1-2):229–244.

[Jha and Lipton 2018b] Jha, P. K. and Lipton, R. (2018b). Numerical convergence of nonlinear nonlocal continuum models to local elastodynamics. *International Journal for Numerical Methods in Engineering* ,114(13):1389–1410.

[Jha and Lipton, 2018a] Jha, P. K. and Lipton, R. (2018a). Numerical analysis of nonlocal fracture models in Hölder space. *SIAM J. Numer. Anal.*, 56: 906–941.

[Jha and Lipton, 2019b] Jha, P. K. and Lipton, R. (2019b). Small horizon limit of state based peridynamic models. *In preparation.*

[Jha and Lipton, 2019a] Jha, P. K. and Lipton, R., 2019a. Numerical convergence of finite difference approximations for state based peridynamic fracture models. Comput. Methods. Appl. Mech. Engrg. 351, 184–225.

[Jha and Lipton, 2019] Jha, P. K. and Lipton, R. (2019). Finite element convergence for state-based peridynamic fracture models. *To appear in Communications in Applied Mathematics and Computation, 2019.*

[Karaa, 2012] Karaa, S. (2012). Stability and convergence of fully discrete finite element schemes for the acoustic wave equation. *Journal of Applied Mathematics and Computing*, 40(1-2):659–682.

[Kostrov and Nikitin(1970)] Kostrov, B. V. and Nikitin, L. V., 1970. Some general problems of mechanics of brittle fracture. Arch. Mech. Stosowanej. 22, 749–775.

[Lipton, 2014] Lipton, R. (2014) Dynamic brittle fracture as a small horizon limit of peridynamics. *Journal of Elasticity*, 117:21–50.

[Lipton, 2016] Lipton, R. (2016). Cohesive dynamics and brittle fracture. *Journal of Elasticity*, 124(2):143–191.

[Lipton et al., 2018a] Lipton, R., Said, E., and Jha, P. (2018a). Free damage propagation with memory. *Journal of Elasticity*, 133(2):129–153.

[Lipton et al., 2018b] Lipton, R., Said, E., and Jha, P. K. (2018b). Dynamic brittle fracture from nonlocal double-well potentials: A state-based model. *Handbook of Nonlocal Continuum Mechanics for Materials and Structures*, pages 1–27.

[Lipton et al., 2016] Lipton, R., Silling, S., and Lehoucq, R. (2016). Complex fracture nucleation and evolution with nonlocal elastodynamics. *arXiv preprint arXiv:1602.00247.*

[Lipton and Jha, 2019] Lipton, R., and Jha, P. (2019). Classic dynamic fracture recovered as the limit of a nonlocal peridynamic model: The single edge notch in tension. *arXiv preprint arXiv:1908.07589.*

[Littlewood, 2010] Littlewood, D. J. (2010). Simulation of dynamic fracture using peridynamics, finite element modeling, and contact. In *Proceedings of the ASME 2010 International Mechanical Engineering Congress and Exposition (IMECE).*

[Macek and Silling, 2007] Macek, R. W. and Silling, S. A. (2007). Peridynamics via finite element analysis. *Finite Elements in Analysis and Design*, 43(15):1169–1178.

[Mengesha and Du, 2015] Mengesha, T. and Du, Q. (2015). On the variational limit of a class of nonlocal functionals related to peridynamics. *Nonlinearity*, 28(11):3999.

[Mott, 1948] Mott, N. F. (1948). Fracture in mild steel plates. *Engineering*, 165, 16–18.

[Ren et al., 2017] Ren, B., Wu, C., and Askari, E. (2017). A 3d discontinuous galerkin finite element method with the bond-based peridynamics model for dynamic brittle failure analysis. *International Journal of Impact Engineering*, 99:14–25.

[Silling et al., 2010] Silling, S., Weckner, O., Askari, E., and Bobaru, F. (2010). Crack nucleation in a peridynamic solid. *International Journal of Fracture*, 162(1-2):219–227.

[Silling, 2000] Silling, S. A. (2000). Reformulation of elasticity theory for discontinuities and long-range forces. *Journal of the Mechanics and Physics of Solids*, 48(1):175–209.

[Silling and Bobaru, 2005] Silling, S. A. and Bobaru, F. (2005). Peridynamic modeling of membranes and fibers. *International Journal of Non-Linear Mechanics*, 40(2):395–409.

[Silling et al., 2007] Silling, S. A., Epton, M., Weckner, O., Xu, J., and Askari, E. (2007). Peridynamic states and constitutive modeling. *Journal of Elasticity*, 88(2):151–184.

[Silling and Lehoucq, 2008] Silling, S. A. and Lehoucq, R. B. (2008). Convergence of peridynamics to classical elasticity theory. *Journal of Elasticity*, 93(1):13–37.

[Tian and Du, 2014] Tian, X. and Du, Q. Asymptotically compatible schemes and applications to robust discretization of nonlocal models. *SIAM J. Numer. Anal.*, 52-4 (2014), pp. 1641–1665.

[Weckner and Abeyaratne, 2005] Weckner, O. and Abeyaratne, R. (2005). The effect of long-range forces on the dynamics of a bar. *Journal of the Mechanics and Physics of Solids*, 53(3):705–728.

[Willis(1975)] Willis, J. R., 1975, Equations of motion for propagating cracks, The mechanics and physics of fracture, The Metals Society. 57–67.